Simulations of turbulent rotating flows using a subfilter scale stress model derived from the partially integrated transport modeling method

Bruno Chaouat[a)]
ONERA, 92322 Châtillon, France

(Received 4 January 2012; accepted 29 February 2012; published online 23 April 2012)

The partially integrated transport modeling (PITM) method [B. Chaouat and R. Schiestel, "A new partially integrated transport model for subgrid-scale stresses and dissipation rate for turbulent developing flows," Phys. Fluids **17**, 065106 (2005); R. Schiestel and A. Dejoan, "Towards a new partially integrated transport model for coarse grid and unsteady turbulent flow simulations," Theor. Comput. Fluid Dyn. **18**, 443 (2005); B. Chaouat and R. Schiestel, "From single-scale turbulence models to multiple-scale and subgridscale models by Fourier transform," Theor. Comput. Fluid Dyn. **21**, 201 (2007); B. Chaouat and R. Schiestel, "Progress in subgrid-scale transport modelling for continuous hybrid non-zonal RANS/LES simulations," Int. J. Heat Fluid Flow **30**, 602 (2009)] viewed as a continuous approach for hybrid RANS/LES (Reynolds averaged Navier-Stoke equations/large eddy simulations) simulations with seamless coupling between RANS and LES regions is used to derive a subfilter scale stress model in the framework of second-moment closure applicable in a rotating frame of reference. This present subfilter scale model is based on the transport equations for the subfilter stresses and the dissipation rate and appears well appropriate for simulating unsteady flows on relatively coarse grids or flows with strong departure from spectral equilibrium because the cutoff wave number can be located almost anywhere inside the spectrum energy. According to the spectral theory developed in the wave number space [B. Chaouat and R. Schiestel, "From single-scale turbulence models to multiple-scale and subgrid-scale models by Fourier transform," Theor. Comput. Fluid Dyn. **21**, 201 (2007)], the coefficients used in this model are no longer constants but they are some analytical functions of a dimensionless parameter controlling the spectral distribution of turbulence. The pressure-strain correlation term encompassed in this model is inspired from the nonlinear SSG model [C. G. Speziale, S. Sarkar, and T. B. Gatski, "Modelling the pressure-strain correlation of turbulence: an invariant dynamical systems approach," J. Fluid Mech. **227**, 245 (1991)] developed initially for homogeneous rotating flows in RANS methodology. It is modeled in system rotation using the principle of objectivity. Its modeling is especially extended in a low Reynolds number version for handling non-homogeneous wall flows. The present subfilter scale stress model is then used for simulating large scales of rotating turbulent flows on coarse and medium grids at moderate, medium, and high rotation rates. It is also applied to perform a simulation on a refined grid at the highest rotation rate. As a result, it is found that the PITM simulations reproduce fairly well the mean features of rotating channel flows allowing a drastic reduction of the computational cost in comparison with the one required for performing highly resolved LES. Overall, the mean velocities and turbulent stresses are found to be in good agreement with the data of highly resolved LES [E. Lamballais, O. Metais, and M. Lesieur, "Spectral-dynamic model for large-eddy simulations of turbulent rotating flow," Theor. Comput. Fluid Dyn. **12**, 149 (1998)]. The anisotropy character of the flow resulting from the rotation effects is also well reproduced in accordance with

a)Senior Scientist, Computational Fluid Dynamics Department. Electronic mail: Bruno.Chaouat@onera.fr.

1070-6631/2012/24(4)/045108/35/$30.00

the reference data. Moreover, the PITM2 simulations performed on the medium grid predict qualitatively well the three-dimensional flow structures as well as the longitudinal roll cells which appear in the anticyclonic wall-region of the rotating flows. As expected, the PITM3 simulation performed on the refined grid reverts to highly resolved LES. The present model based on a rational formulation appears to be an interesting candidate for tackling a large variety of engineering flows subjected to rotation. [http://dx.doi.org/10.1063/1.3701375]

I. INTRODUCTION

Numerous applications in turbomachinery industry are concerned with flows in system rotation and in the most majority of cases, the fluid motion is turbulent because of the high Reynolds number values. Within the turbine blades, the typical Reynolds number value is of order 0.50×10^5 for a coolant flow passage of about 2 mm diameter.[7] The flow within a turbine blade is of very complex physics because of the Coriolis forces that act both directly on the mean flow and on the turbulent fluctuations. With the aim to investigate the modification of the turbulence by the Coriolis forces, it is more convenient from a physical point of view to consider a flow in a simple geometry such as the flow between infinite parallel plates. In such configuration of laboratory flows, fully developed turbulent channel flows subjected to a spanwise rotation as shown by Figure 1 have been previously studied both experimentally by Johnston *et al.*[8] and numerically by several authors. Such rotating channel flows have been initially computed in the past by using the RANS (Reynolds averaged Navier-Stoke equations) methodology. In particular, Launder *et al.*,[7] Pettersson and Andersson,[9] Chaouat[10] as well as Jakirlic *et al.*[11] performed numerical simulations by using Reynolds stress models (RSM) whereas Gatski and Speziale,[12] Gatski and Wallin,[13] Jongen *et al.*,[14] and Hamba[15] have applied algebraic stress models, both of these models being based on second-moment closures (SMC).[16] Thanks to the increase of computer power, Kristoffersen and Andersson,[17] Lamballais *et al.*,[18] Wu and Kasagi,[19] and more recently, Grundestam *et al.*,[20] and Brethouwer *et al.*,[21] then performed direct numerical simulations (DNS) whereas Tafti and Vanka,[22] Piomelli and Liu,[23] and Lamballais *et al.*,[6] performed large eddy simulations (LES) at higher Reynolds number for investigating the mean features of these turbulent rotating flows by using different subgrid models. Tafti and Vanka[22] performed LES simulations using the Smagorinsky model (SM), Piomelli and Liu[23] applied a dynamic Smagorinsky model (DSM) whereas Lamballais *et al.*[6] used a spectral dynamic model based on the structure function.[24] The characteristics of these previous DNS and LES simulations are summarized in Table I for different Reynolds and rotation numbers, respectively, defined by $R_m = u_m\delta/\nu$ and $R_o = \Omega\delta/u_m$, based on the bulk velocity u_m and the channel width δ, where Ω characterizes the rotation rate. These experimental and numerical studies have shown that the Coriolis forces associated with the rotation appreciably affect the mean motion and the turbulent fluctuations. In particular, as the rotation rate increases, the mean flow becomes more and more asymmetric with respect to the channel center and the turbulence activity dramatically decreases

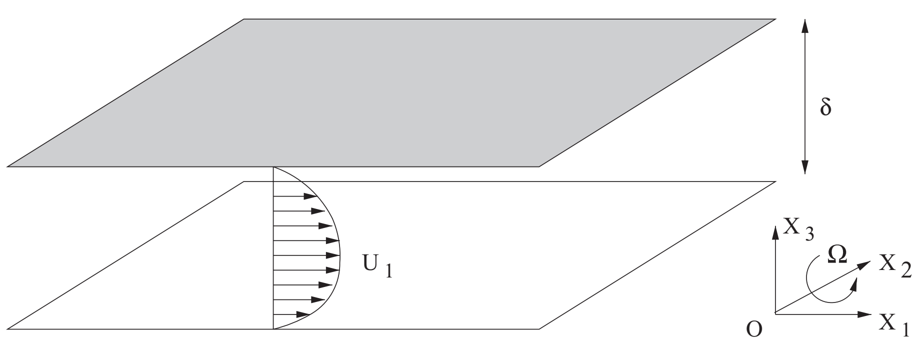

FIG. 1. Schematic of fully-developed turbulent channel flow in a rotating frame.

TABLE I. Characteristics of relevant direct and large-eddy simulations of rotating channel flows $R_m = u_m\delta/\nu$, $R_o = \Omega\delta/u_m$ where δ is the channel width and x_1,x_2,x_3 denotes the axes in the streamwise, spanwise, and normal directions.

Author(s)	Simulation	R_m	R_o	Domain dimensions	Resolution
Lamballais *et al.*[6]	DNS	5000	0.17, 0.50, 1.50	$2\pi\delta \times \pi\delta \times \delta$	$128 \times 180 \times 129$
Kristoffersen and Andersson[17]	DNS	5800	0.50	$2\pi\delta \times \pi\delta \times \delta$	$128 \times 128 \times 128$
Wu and Kasagi[19]	DNS	4560	0.30, 0.50, 0.70,1	$\frac{5}{2}\pi\delta \times \pi\delta \times \delta$	$128 \times 128 \times 97$
Grundestam *et al.*[20]	DNS	5000	0.98, 1.15, 1.21	$2\pi\delta \times \pi\delta \times \delta$	$192 \times 160 \times 129$
	DNS	5000	1.27, 1.50, 1.69	$2\pi\delta \times \pi\delta \times \delta$	$192 \times 160 \times 161$
	DNS	5000	2.06, 2.49, 3.0	$2\pi\delta \times \pi\delta \times \delta$	$192 \times 160 \times 201$
Brethouwer *et al.*[21]	DNS	40 000	0.15, 0.45, 0.9, 1.2	$4\pi\delta \times \frac{3}{2}\pi\delta \times \delta$	$2048 \times 1536 \times 361$
	DNS	60 000	1.5, 2.1, 2.4	$4\pi\delta \times \frac{3}{2}\pi\delta \times \delta$	$1024 \times 768 \times 193$
Piomelli and Liu[23]	DNS	5700	0.144	$2\pi\delta \times \frac{2}{3}\pi\delta \times \delta$	$96 \times 128 \times 97$
Lamballais *et al.*[6]	LES	14 000	0.17, 0.50, 1.50	$\pi\delta \times \frac{1}{2}\pi\delta \times \delta$	$128 \times 64 \times 97$
Tafti and Vanka[22]	LES	5600	0.20, 1	$\pi\delta \times \pi\delta \times \delta$	$64 \times 64 \times 64$
Piomelli and Liu[23]	LES	11 500	0.21	$2\pi\delta \times \frac{2}{3}\pi\delta \times \delta$	$48 \times 64 \times 64$
	LES	23 500	0.21	$2\pi\delta \times \frac{2}{3}\pi\delta \times \delta$	$48 \times 64 \times 64$
Chaouat (present work)	PITM	14 000	0.17, 0.50, 1.50	$3\delta \times 2\delta \times \delta$	$24 \times 48 \times 64$
	PITM	14 000	0.17, 0.50, 1.50	$3\delta \times 2\delta \times \delta$	$84 \times 64 \times 64$
	PITM	14 000	1.50	$3\delta \times 2\delta \times \delta$	$124 \times 84 \times 84$

with respect to the non-rotating case, the decrease being more pronounced in the cyclonic region than in the anticyclonic wall region. As a result of interest, these studies have indicated that the rotation stabilizes the cyclonic region of the channel flow whereas it destabilizes the anticyclonic region.[6,8,18] Moreover, at very high rotation regime, the turbulent flows may relaminarize because of the rotating effects. From a quantitative point of view, experimental flow visualizations[8] as well as recent direct numerical simulations[6,17] have provided the structural information on the flow.

Direct numerical simulations constitute the best numerical tool for investigating turbulent rotating flows but they are only affordable at very low Reynolds number because of the high CPU time consuming. Large eddy simulations which consist of modeling the more universal small scales corresponding to the region of the spectrum located after the cutoff wave number κ_c while the resolved scales are explicitly computed by the numerical scheme are a promising method. These simulations allow to mimic the acting mechanisms of turbulent interactions. However, most of LES simulations are performed by using subgrid eddy viscosity models[24–27] that assume a direct constitution relation between the turbulent stress and strain components, only valid for fine grained turbulence. As a consequence, these simulations are accurate only if they are performed on refined grids imposing that the cutoff wave number is placed in the inertial zone of the spectrum. But this stringent criterion cannot be satisfied for industrial applications requiring large computational domain like, for instance, the entire aircraft which remains out of scope of LES.[28] This problem is particularly acute at high turbulent Reynolds number since the Kolmogorov scale decreases according to the $R_t^{-9/4}$ law. As for direct numerical simulations, even with the rapid increase in computer speed and the use of parallelization techniques in computational fluid dynamics (CFD) codes,[28,29] LES simulations remain not affordable in practice. On the other hand, the RANS approach including second-moment closure models as, for instance, those described in Refs. 5 and 30–33 appears well suited for predicting engineering flows without requiring prohibitive computation times. Second-moment closure models are able to simulate turbulent flows in system rotation because the Coriolis forces are naturally embodied in the transport equations for the individual Reynolds stress components,[10,34] contrary to standard first-order closure models (including in their formulations constant coefficients and assuming the Boussinesq hypothesis) which are unable to "see" the rotation. Viscosity models require explicit corrections to account for the rotation.[35–37] However, the RANS method based on a statistical averaging or in practice, as recalled by Gatski *et al.*,[38] a long-time averaging which is sufficiently large in comparison with the turbulence time scale, is not well suited for simulating unsteady flows subjected to a large range of frequencies that can interact with the turbulence time scale.

As mentioned by Germano,[39] the new trend in turbulence modeling is to bridge the gap between the RANS and LES approaches that have been developed independently from each other, referring to their basic physical foundations. Hybrid RANS/LES methods capable of reproducing a RANS-type behavior in the vicinity of a solid boundary and a LES-type behavior far away from the wall boundary have been proposed in the last decade.[40–42] According to the literature,[38] hybrid methods can be classified into two categories, zonal and non-zonal methods. RANS/LES zonal methods rely on two different models, a RANS model and a subgrid-scale model, which are applied in different domains separated by an interface whereas non-zonal methods assume that the governing set of equations is smoothly transitioning from a RANS behavior to a LES behavior, based on criteria updated during the computation. An updated review can be found in Ref. 41, the noncommutativity between the hybrid filter and the spatial derivative of the hybrid-filtered equations being studied in Ref. 43. Among these hybrid RANS/LES methods, the detached eddy simulation developed by Spalart and co-authors[28,44] is one of the most popular models. In this line of thought, Chaouat and Schiestel,[1,3,4] Schiestel and Dejoan[2] have recently developed the partially integrated transport modeling (PITM) method viewed as a continuous approach for hybrid RANS/LES simulations with seamless coupling between the RANS and LES regions. This method is particularly relevant for studying turbulent flows with non-standard spectral distributions with some departure from the Kolmogorov spectrum.[1–4,45] From a theoretical point of view, the PITM method gains major interest because it bridges these two different levels of description in a consistent way by a unifying formalism developed in the spectral space.[3] As the transport equations for the subfilter stress in terms of central moment[46] are formally similar to the statistical equations, the PITM method can be applied to almost all statistical models to derive their hybrid LES counterparts corresponding to subfilter models, provided an adequate dissipation equation is coupled to the turbulent energy or stress transport equations. These derived subfilter models include both eddy viscosity models[2,47] and stress models,[1,4,45,48,49] depending on the level of closure. These models have been previously used for successfully simulating engineering flows performed on coarse grids providing the instantaneous flow structures with qualitative agreement with DNS.[1,2,4,45,48–50] In the last several years, the PITM method has become more and more widespread in turbulence modeling[1,49–52] because of its practical interest in the field of engineering applications. But these derived stress transport models require a specific modeling to tackle engineering flows encountered in turbomachinery industry because of the rotation effects.

In this work, considering that second-moment closures (SMC) constitute a convenient framework for system rotation, we propose to derive a specific subfilter scale stress model taking into account the advanced modeled redistribution term developed in RANS methodology by Speziale *et al.*[5] denoted SSG. This modeling strategy is motivated by the idea that the recognized advantages of second-moment closures are worth to be transposed to subfilter-scale modeling when the subfilter scale (SFS) part is not small compared to the resolved part. To this aim, we will show that the Coriolis term must be embedded in the subfilter stress model as a source term and that the pressure-strain-correlation term which plays a pivotal role by redistributing the turbulent energy among the different stress components can be developed in an invariant form under arbitrary time-dependent rotations of the spatial frame of reference satisfying the concept of objectivity,[16] if some approximations are, however, conceded. As a result of the modeling, we will derive a specific subfilter scale stress model accounting for the rotation and complemented with low Reynolds number extensions that embodies interesting features allowing a more realistic description of the flow anisotropy than eddy viscosity models, and also a better account of history and nonlocal effects. Numerical PITM simulations of channel flows subject to a spanwise rotation will be then performed for illustrating the potentials of the present model, the objective being to show that the model is able to accurately simulate rotating flows on very coarse grids with quasi-similar results for the mean velocity and turbulent stresses as those obtained by highly resolved LES (Refs. 6 and 18) performed on refined grids. In this study, the coarse grids are deliberately chosen to highlight the ability of the PITM method to simulate large scales of the flow with a sufficient fidelity for engineering computations. Hence, the focus of this article will not be mainly the description of the flow physics, which have been studied in the cited references, but also the response of the subfilter scale stress scale model to the physical phenomena involving in rotating flows at moderate, medium, and high rotation rates.

II. THE FILTERING PROCESS AND GOVERNING EQUATIONS

We consider the turbulent flow of a viscous incompressible fluid. In a frame rotating at angular velocity $\mathbf{\Omega}(t)$, the instantaneous Navier-Stokes equations read[53]

$$\frac{\partial u_j}{\partial x_j} = 0, \tag{1}$$

$$\frac{\partial u_i}{\partial t} + \frac{\partial}{\partial x_j}\left(u_i u_j\right) = -\frac{1}{\rho}\frac{\partial p}{\partial x_i} + \nu \frac{\partial^2 u_i}{\partial x_j \partial x_j} - 2\epsilon_{ijk}\Omega_j u_k - \epsilon_{ijk}\epsilon_{kpq}\Omega_j\Omega_p x_q - \epsilon_{ijk}\dot{\Omega}_j x_k - \dot{U}_0, \tag{2}$$

where u_i, $\dot{U}_0$, p, ϵ_{ijk}, ν are the velocity vector, translational acceleration of the non-inertial framing, the pressure, the Levi-Civita's permutation tensor, the kinematic viscosity of the fluid, respectively. The terms appearing in the right-hand side of this equation are referred to as the Coriolis acceleration $-2\mathbf{\Omega} \times \boldsymbol{u}$, centrifugal acceleration $-\mathbf{\Omega} \times (\mathbf{\Omega} \times \boldsymbol{x})$, Eulerian acceleration $-\dot{\mathbf{\Omega}} \times \boldsymbol{x}$, and translational acceleration $-\dot{\boldsymbol{U}}_{\mathbf{0}}$. In large eddy simulations, the flow variable ϕ is decomposed into a resolved scale part $\bar{\phi}$ (filtered part) including the statistical mean $\langle\phi\rangle$ and the large scale $\phi^< = \bar{\phi} - \langle\phi\rangle$ and a subfilter-scale (or modeled) fluctuating part ϕ'. The filtered variable $\bar{\phi}$ is defined by the filter function G_Δ as

$$\bar{\phi}(\boldsymbol{x}) = \iiint_{\mathcal{D}} G_\Delta(\boldsymbol{x} - \boldsymbol{x}')\,\phi(\boldsymbol{x}')\,d^3x', \tag{3}$$

where Δ is the filter width. Assuming that the filter commutes with the differential operators, the filtering operation is applied to the instantaneous Navier-Stokes equations and yields the filtered equations of motion in a frame rotating at angular velocity $\mathbf{\Omega}(t)$:[54]

$$\frac{\partial \bar{u}_j}{\partial x_j} = 0, \tag{4}$$

$$\frac{\partial \bar{u}_i}{\partial t} + \frac{\partial}{\partial x_j}\left(\bar{u}_i \bar{u}_j\right) = -\frac{1}{\rho}\frac{\partial \bar{p}}{\partial x_i} + \nu \frac{\partial^2 \bar{u}_i}{\partial x_j \partial x_j} - \frac{\partial (\tau_{ij})_{SFS}}{\partial x_j} - 2\epsilon_{ijk}\Omega_j\bar{u}_k - \epsilon_{ijk}\epsilon_{kpq}\Omega_j\Omega_p x_q$$
$$-\epsilon_{ijk}\dot{\Omega}_j x_k - \dot{U}_0, \tag{5}$$

where $(\tau_{ij})_{SFS}$ denotes the subfilter-scale stress tensor defined by the mathematical relation

$$(\tau_{ij})_{SFS} = \overline{u_i u_j} - \bar{u}_i \bar{u}_j. \tag{6}$$

The presence of the turbulent contribution $(\tau_{ij})_{SFS}$ in Eq. (5) indicates the effect of the subfilter scales to the resolved field. The resolved scale tensor is computed by the relation

$$(\tau_{ij})_{LES} = \bar{u}_i \bar{u}_j - \langle u_i\rangle\langle u_j\rangle. \tag{7}$$

Assuming that the large and small scale fluctuations are uncorrelated as for spectral cutoff filter defined by the Fourier transform,[55,56] the total stress τ_{ij} then reads[3]

$$\tau_{ij} = \langle(\tau_{ij})_{SFS}\rangle + \langle(\tau_{ij})_{LES}\rangle, \tag{8}$$

whereas the statistical turbulent energy is obtained as half the trace of Eq. (8)

$$k = \langle k_{SFS}\rangle + \langle k_{LES}\rangle\,. \tag{9}$$

As usually made in LES simulations, the statistical average of the resolved stress $\langle(\tau_{ij})_{LES}\rangle$ which corresponds to the correlation of the large scale fluctuating velocities appearing in Eq. (7) is computed by a numerical procedure using the relation

$$\langle(\tau_{ij})_{LES}\rangle = \langle u_i^< u_j^<\rangle = \langle\bar{u}_i\bar{u}_j\rangle - \langle\bar{u}_i\rangle\langle\bar{u}_j\rangle, \tag{10}$$

where $u_i^< = \bar{u}_i - \langle u_i \rangle$ denotes the large scale fluctuating velocity. Its transport equation is given by

$$\frac{\partial u_i^<}{\partial t} + \frac{\partial}{\partial x_j}\Big(\bar{u}_i\bar{u}_j - \langle u_i\rangle\langle u_j\rangle\Big) = -\frac{1}{\rho}\frac{\partial p^<}{\partial x_i} + \nu\frac{\partial^2 u_i^<}{\partial x_j \partial x_j} - \frac{\partial}{\partial x_j}\Big((\tau_{ij})_{SFS} - \tau_{ij}\Big) - 2\epsilon_{ijk}\Omega_j u_k^<, \tag{11}$$

whereas the transport equation for the subfilter-scale fluctuation u_i' reads

$$\frac{\partial u_i'}{\partial t} + \frac{\partial}{\partial x_j}\Big(u_i u_j - \bar{u}_i\bar{u}_j\Big) = -\frac{1}{\rho}\frac{\partial p'}{\partial x_i} + \nu\frac{\partial^2 u_i'}{\partial x_j \partial x_j} + \frac{\partial (\tau_{ij})_{SFS}}{\partial x_j} - 2\epsilon_{ijk}\Omega_j u_k' \tag{12}$$

or equivalently,

$$\frac{\partial u_i'}{\partial t} + \bar{u}_j\frac{\partial u_i'}{\partial x_j} = -u_j'\frac{\partial \bar{u}_i}{\partial x_j} - u_j'\frac{\partial u_i'}{\partial x_j} - \frac{1}{\rho}\frac{\partial p'}{\partial x_i} + \nu\frac{\partial^2 u_i'}{\partial x_j \partial x_j} + \frac{\partial (\tau_{ij})_{SFS}}{\partial x_j} - 2\epsilon_{ijk}\Omega_j u_k'. \tag{13}$$

Equations (11) and (12) show that the large and subfilter scale fluctuating velocities are only affected by the frame of reference through the Coriolis acceleration. The closure of the filtered momentum Eq. (5) requires to model the subfilter-scale turbulent stress $(\tau_{ij})_{SFS}$. In the framework of second-moment turbulence closures, this is made by means of its transport equation which is the required level for accurately reproducing the physical processes of turbulent flows. Like in the statistical modeling, the closure of the filtered momentum equation requires also to model the tensorial subfilter dissipation rate $(\epsilon_{ij})_{SFS}$ that appears in the right-hand side of this equation or in a simple approach, the scalar dissipation rate ϵ_{SFS}. In the present case, ϵ_{SFS} is modeled by means of its transport equation which is derived itself from the PITM method. The modeling of the transport equation for ϵ_{SFS} constitutes the main ingredient of the PITM approach and allows to obtain an accurate value of the energy dissipation-rate even in situation of non-equilibrium flows when the grid size is no longer a good estimate of the characteristic turbulence length-scale.

III. PARTIALLY INTEGRATED TRANSPORT MODELING METHOD

A. Principle of the method

From a physical standpoint, the PITM method finds its basic foundation in the spectral space by considering the Fourier transform of the two-point fluctuating velocity correlation equations in homogeneous turbulence. The extension to non-homogeneous turbulence is developed easily within the approximate framework of the tangent homogeneous space at a point of a non-homogeneous flow field assuming Taylor series expansion in space for the mean velocity field.[3,57] Indeed, this concept ensures that the filtered field goes to the statistical mean field when the filter width goes to infinity. In particular, when the cutoff wave number vanishes, the full integration in the tangent homogeneous space exactly corresponds to the statistical mean, that guarantees exact compatibility with RANS equations.[3] When transposing the spectral equation in the physical space by inverse Fourier transform involving partial integration of the turbulence field in the range $[\kappa_c, \kappa_d]$ where $\kappa_c = \pi/\Delta$ is the cutoff wave number computed by the grid size width Δ, and κ_d is the dissipative wave number placed at the end of the inertial range of the spectrum completely after the transfer zone assuming that the energy pertaining to higher wave numbers is entirely negligible, one can derive a subfilter-scale model based on the transport equations for the subfilter scale stresses $(\tau_{ij})_{SFS}$ and the dissipation rate ϵ_{SFS} that look formally like the corresponding RANS/RSM model but the coefficients used in the model are no longer constants.[3] They are now some functions of the dimensionless parameter η_c

$$\eta_c = \kappa_c L_e = \frac{\pi\, L_e}{\Delta}, \tag{14}$$

involving the cutoff wave number κ_c and the turbulent length scale L_e

$$L_e = \frac{k^{3/2}}{(\langle\epsilon_{SFS}\rangle + \langle\epsilon^<\rangle)} \tag{15}$$

built using the total turbulent kinetic energy k, the subfilter dissipation rate ϵ_{SFS}, and the large scale dissipation rate denoted $\epsilon^<$

$$\epsilon^< = \nu \overline{\frac{\partial u_i^<}{\partial x_j} \frac{\partial u_i^<}{\partial x_j}}. \tag{16}$$

In Eq. (14), the quantity Δ is the effective filter accounting for the anisotropy of the grid near the walls like the proposal of Scotti[58]

$$\Delta = \Delta_a \left(\zeta + (1-\zeta) \frac{\Delta_b}{\Delta_a} \right), \tag{17}$$

where the filters Δ_a and Δ_b are defined by $\Delta_a = (\Delta_1 \Delta_2 \Delta_3)^{1/3}$ and $\Delta_b = (\Delta_1^2 + \Delta_2^2 + \Delta_3^2)/3)^{1/2}$ and where ζ is a constant parameter. In PITM methodology, the subfilter-scale stress model varies continuously with respect to the ratio of the turbulent length-scale to the grid-size L_e/Δ. For the limiting condition when the parameter η_c goes to zero, the subfilter-scale model behaves like a RANS/RSM model whereas when η_c goes to infinity, the computation switches to DNS if the grid-size is enough refined. This model property can be proved easily. The PITM method has been developed in a such way that the functional coefficients used in the subfilter models take on the RANS values $c_{SFS\epsilon_2} = c_{\epsilon_2}$ when η_c reduces to zero implying that the RANS model is formally recovered in a such limit. In practice, when performing PITM simulations, the parameter η_c evolves in time and space and goes to zero only in certain flow regions like in the near wall region, for instance. In the core flow far away the wall regions, the grid-size is often of coarse resolution but η_c usually still reaches large values because of the turbulence length-scale L_e which appreciably increases allowing the PITM method to simulate a certain degree of unsteadiness for large scales. As a result, previous PITM simulations performed on very coarse meshes have revealed that the PITM simulations still provide better predictions than pure RANS models.[1,45] This success seems to be attributed to the ability of the hybrid model to capture the large-scales dynamics of the flow, particularly in the shear layer regions, that play a pivotal role in the turbulent mechanisms.[2,45,47] On the other hand, when η_c is very large, the subfilter model goes to the Smagorinsky model as demonstrated in Refs. 4 and 49 using spectral equilibrium equations. When the parameter η_c goes to infinity, the coefficient $c_{SFS\epsilon_2}$ reaches the value c_{ϵ_1}. In this case, previous computations[1] have shown in practice that the subgrid energy cannot be maintained implying that the model becomes useless. These results are consistent with previous numerical simulations showing the behavior of the PITM method in the case of decay of isotropic turbulence using a subfilter viscosity model[2] or a subfilter scale stress model.[4] In particular, it has been demonstrated in Ref. 2 that the PITM method preserves the concept of the energy cascading process as free of any spectral cutoff location. The PITM method has been initially developed in aiming to perform continuous hybrid non-zonal RANS/LES simulations on relatively coarse grids since the cutoff wave number can be located almost anywhere within the energy spectrum, contrary to highly resolved LES that requires a location in the inertial range of the spectrum. In PITM simulations, the contribution of the subfilter scales can be dominant and even represents the main energy in particular flow region. The ratio of the subfilter energy to the resolved energy can be moreover increased by applying a filter width equals, for instance, twice the grid spacing, taking into account that the derived PITM models are subfilter models and not only subgrid models. Whatever the subfilter scale energy compared to the resolved energy, the subfilter scale stresses and the dissipation-rate are computed by transport equations while the large scales are explicitly resolved by the numerical scheme, so that the usual hypothesis of local isotropy prevailing for fine grained turbulence is not anymore necessary. This is the main argument that differentiates conventional LES simulations to PITM simulations. Note that a formalism based on temporal filtering has been proposed recently to handle non-homogeneous stationary flows leading to a variant of the PITM method using temporal filters and called TPITM (temporal partially integrated transport modeling) method.[48] As a result of the modeling developed in the frequency space, the dissipation rate equation finally takes the same formulation as the one found in the spectral space by the PITM method. The PANS (partially averaged Navier-Stokes) method[59] recently emerged for performing unsteady computations also appears in the line of thought of the PITM method. The final PANS equations have great similarities with the PITM equations, despite a completely different argumentation and significant differences in the practical details. With regard to the PITM method, the PANS method, however, imposes an arbitrary fixed ratio $\langle k_{SFS}\rangle/k$ of the modeled energy to the total energy whereas in the PITM method, it is dynamically computed according to the physics of turbulence.

B. Exact transport equations in the presence of rotation

The first step of the present approach consists of writing the exact transport equation of the subfilter-scale stress $(\tau_{ij})_{SFS}$ in presence of the rotation. Following the work of Germano,[46] it appears that the transport equation for the subfilter-scale stress takes a generic form if written in terms of central moments. By using the material derivative operator $D/Dt = \partial/\partial t + \bar{u}_k \partial/\partial x_k$, the transport equation of the subfilter stress tensor can be therefore written in the simple compact form as

$$\frac{D(\tau_{ij})_{SFS}}{Dt} = P_{ij} + \Pi_{ij} + J_{ij} - (\epsilon_{ij})_{SFS}, \tag{18}$$

where the terms appearing in the right-hand side of this equation are identified as production, redistribution, diffusion, and dissipation. The transport equation for the subfilter energy is obtained as the half trace of Eq. (18)

$$\frac{Dk_{SFS}}{Dt} = P + J - \epsilon_{SFS}, \tag{19}$$

where $P = P_{mm}/2$, $J = J_{mm}/2$, and $\epsilon_{SFS} = (\epsilon_{mm})_{SFS}/2$. The production term P_{ij} is composed by the term P^1_{ij} produced by the interaction between the subfilter stress and the filtered gradient velocity

$$P^1_{ij} = -(\tau_{ik})_{SFS}\frac{\partial \bar{u}_j}{\partial x_k} - (\tau_{jk})_{SFS}\frac{\partial \bar{u}_i}{\partial x_k}\,, \tag{20}$$

and by the term P^2_{ij} generated by the rotation involving the Coriolis forces

$$P^2_{ij} = -2\Omega_p\Big(\epsilon_{jpk}(\tau_{ki})_{SFS} + \epsilon_{ipk}(\tau_{kj})_{SFS}\Big). \tag{21}$$

The exact expressions of the redistribution Π_{ij}, diffusion J_{ij}, and dissipation rate ϵ_{ij} appearing on the right-hand side of Eq. (18) are the following:

$$\Pi_{ij} = \frac{2}{\rho}\,\Phi\left(p, S_{ij}\right)\,, \tag{22}$$

$$J_{ij} = -\frac{\partial \Phi(u_i, u_j, u_k)}{\partial x_k} - \frac{1}{\rho}\frac{\partial \Phi(p, u_i)}{\partial x_j} - \frac{1}{\rho}\frac{\partial \Phi(p, u_j)}{\partial x_i} + \nu\frac{\partial^2 \Phi(u_i, u_j)}{\partial x_k \partial x_k}\,, \tag{23}$$

$$(\epsilon_{ij})_{SFS} = 2\nu\,\Phi\left(\frac{\partial u_i}{\partial x_k}, \frac{\partial u_j}{\partial x_k}\right), \tag{24}$$

where in Eqs. (22)–(24), the functions Φ of two or three variables are defined by

$$\Phi(f, g) = \overline{fg} - \bar{f}\bar{g}, \tag{25}$$

and

$$\Phi(f, g, h) = \overline{fgh} - \bar{f}\Phi(g, h) - \bar{g}\Phi(h, f) - \bar{h}\Phi(f, g) - \bar{f}\bar{g}\bar{h} \tag{26}$$

applicable for any turbulent quantities f, g, h. The quantity S_{ij} appearing in Eq. (22) denotes the strain deformation

$$S_{ij} = \frac{1}{2}\left(\frac{\partial u_i}{\partial x_j} + \frac{\partial u_j}{\partial x_i}\right). \tag{27}$$

Contrary to the production term P_{ij} which is exact, the redistribution, diffusion, and dissipation terms need to be modeled in the range wave number $[\kappa_c, \kappa_d]$. The present formalism shows clearly the formal analogy between the statistical and filtered approaches and their compatibility. As a consequence, the closure approximations used for the statistical partially averaged equations are assumed to prevail also in the case of large eddy numerical simulations.

C. Modeling of the subfilter-scale stress transport equation in the presence of rotation

As usually made in RANS methodology, the next step is to model the unknown terms appearing in the exact Eq. (18) by means of physical considerations. Beyond the formal analogy existing between the RANS and LES equations, the main hypothesis underlying the development of the PITM method is to assume that the interaction mechanisms of the subfilter-scales with the resolved scales of the turbulence are of the same nature than the interaction mechanisms involving all the fluctuating scales with the mean flow.[4] This hypothesis is so natural that it was already used in the pioneering work of Deardorff[60] allowing transposition of closure hypotheses from RANS to LES. In a practical point of view, this means that the subfilter model as a function of the parameter η_c can be inspired from the RANS model provided it goes to the RANS limit when η_c goes to zero. For η_c different from zero, a modification of the length/time scales must be applied to account for LES. This strategy is adopted to model the pressure-strain correlation term Π_{ij} which redistributes the turbulent energy among the stress components. In the case of PITM simulations performed on coarse grids, Π_{ij} reduces to the pressure-strain subfilter fluctuating correlations

$$\Pi_{ij} = 2\Phi(p, S_{ij})/\rho = 2(\overline{pS_{ij}} - \bar{p}\overline{S_{ij}})/\rho = \frac{2}{\rho}\left(\overline{\bar{p}\bar{S}_{ij}} - \bar{p}\bar{S}_{ij} + \overline{\bar{p}S'_{ij}} + \overline{p'\bar{S}_{ij}} + \overline{p'S'_{ij}}\right) \approx 2\overline{p'S'_{ij}}/\rho. \tag{28}$$

From Eq. (12) written in system rotation, on can see that the subfilter-scale fluctuating pressure p' is solution of the Poisson equation that reads

$$\frac{1}{\rho}\frac{\partial^2 p'}{\partial x_i \partial x_i} = -\frac{\partial^2}{\partial x_j \partial x_i}\left[u'_i u'_j - (\tau_{ij})_{SFS}\right] - 2\left(\frac{\partial \bar{u}_i}{\partial x_j} + \epsilon_{ikj}\Omega_k\right)\frac{\partial u'_j}{\partial x_i}. \tag{29}$$

Like in RANS statistical modeling,[10] when integrating this equation in space in absence of boundaries, using the Green's function solution and then multiplying by the fluctuating strain S'_{ij}, it is found that Π_{ij} can be decomposed into a slow part Π^1_{ij} and a rapid part Π^2_{ij} as follows:

$$\Pi^1_{ij}(\boldsymbol{x}) = \frac{1}{2\pi}\iiint_{\mathcal{D}} \overline{\frac{\partial^2}{\partial x_m \partial x_k}\left[u'_k u'_m - (\tau_{km})_{SFS}\right](\boldsymbol{x}')S'_{ij}(\boldsymbol{x})}\frac{d^3x'}{|\boldsymbol{x}-\boldsymbol{x}'|}, \tag{30}$$

and

$$\Pi^2_{ij}(\boldsymbol{x}) = \frac{1}{\pi}\iiint_{\mathcal{D}} \overline{\left[\left(\frac{\partial \bar{u}_k}{\partial x_m} + \epsilon_{kpm}\Omega_p\right)\frac{\partial u'_m}{\partial x_k}\right](\boldsymbol{x}')S'_{ij}(\boldsymbol{x})}\frac{d^3x'}{|\boldsymbol{x}-\boldsymbol{x}'|}. \tag{31}$$

These equations clearly show that the slow term Π^1_{ij} characterizes the return to isotropy due to the action of turbulence on itself whereas the rapid term Π^2_{ij} describes the return to isotropy by action of the absolute filtered velocity gradient involving the rotation defined by

$$\frac{\partial_a \bar{u}_k}{\partial x_l} = \frac{\partial \bar{u}_k}{\partial x_l} + \epsilon_{kpl}\Omega_p. \tag{32}$$

In the present case, these terms Π^1_{ij} and Π^2_{ij} are modeled assuming that the usual nonlinear statistical SSG Reynolds stress models of Speziale *et al.*[5] must be recovered in the limit of vanishing cutoff wave number κ_c ($\kappa_c \to 0$). The SSG model has been selected because it is well suited for rotating shear flows to which it has been calibrated. The term Π^1_{ij} is modeled as

$$\Pi^1_{ij} = -c_{SFS_1}\epsilon_{SFS}a_{ij} + c_{SFS_2}\epsilon_{SFS}(a_{ik}a_{kj} - \tfrac{2}{3}a_{mn}a_{mn}), \tag{33}$$

where a_{ij} denotes the anisotropy tensor

$$a_{ij} = \frac{(\tau_{ij})_{SFS} - 2/3k_{SFS}\delta_{ij}}{2k_{SFS}}, \tag{34}$$

and where the coefficients c_{SFS_1} and c_{SFS_2} are now some increasing functions of the dimensionless parameter η_c in LES methodology. The use of these functions has the effect to strengthen the return to isotropy in the range of larger wave numbers.[61,62] The second term Π^2_{ij} is modeled by extending the mathematical approach of Speziale *et al.*[5] developed in homogeneous flows in RANS methodology to the LES methodology for rotational frame of reference by taking into account the absolute filtered velocity gradients appearing in Eq. (31) instead of the mean statistical velocity gradient. As a result, the modeled expression Π^2_{ij} takes the form as

$$\Pi^2_{ij} = c_3 k_{SFS}\overline{S}_{ij} + c_4 k_{SFS}\left(a_{ik}\overline{S}_{jk} + a_{jk}\overline{S}_{ik} - \tfrac{2}{3}a_{mn}\overline{S}_{mn}\delta_{ij}\right) + c_5 k_{SFS}\left(a_{ik}\overline{W}_{jk} + a_{jk}\overline{W}_{ik}\right), \quad (35)$$

where the absolute mean strain deformation S_{ij} and the absolute mean vorticity tensor W_{ij} are defined by

$$\overline{S}_{ij} = \frac{1}{2}\left(\frac{\partial_a \bar{u}_i}{\partial x_j} + \frac{\partial_a \bar{u}_j}{\partial x_i}\right) = \frac{1}{2}\left(\frac{\partial \bar{u}_i}{\partial x_j} + \frac{\partial \bar{u}_j}{\partial x_i}\right), \quad (36)$$

and

$$\overline{W}_{ij} = \frac{1}{2}\left(\frac{\partial_a \bar{u}_i}{\partial x_j} - \frac{\partial_a \bar{u}_j}{\partial x_i}\right) = \frac{1}{2}\left(\frac{\partial \bar{u}_i}{\partial x_j} - \frac{\partial \bar{u}_j}{\partial x_i}\right) + \epsilon_{mji}\Omega_m = \omega_{ij} + \epsilon_{mji}\Omega_m, \quad (37)$$

where ω_{ij} denotes the relative vorticity. The rotational effects are taken into account in the redistribution term Π_{ij} through the third term appearing in the right-hand side of Eq. (35) involving the c_5 coefficient due to the presence of the extra term $\epsilon_{mji}\Omega_m$. So that, only the rapid term Π^2_{ij} is modified to account for the rotation. We demonstrate in the Appendix that the exact redistribution term Π_{ij} is an objective tensor whereas its modeling is only an approximation. In Eq. (35), the coefficient c_3, c_4, and c_5 remain as the same coefficients as those used in statistical modeling.[3,63] Physically, this assumption means that the rapid modeled redistribution term in the wave number range $[\kappa_c, \infty[$ remains unaffected by the cutoff wave number κ_c. The diffusion term J_{ij} defined in Eq. (23) accounting to the fluctuating velocities and pressure together with the molecular diffusion is conventionally approximated by the generalized gradient-diffusion hypothesis[64]

$$J_{ij} = \frac{\partial}{\partial x_k}\left(\nu\frac{\partial(\tau_{ij})_{SFS}}{\partial x_k} + c_s\frac{k_{SFS}}{\epsilon_{SFS}}(\tau_{kl})_{SFS}\frac{\partial(\tau_{ij})_{SFS}}{\partial x_l}\right), \quad (38)$$

where c_s is a constant numerical coefficient.

D. Modeling of the subfilter-scale dissipation rate transport equation

Closure of Eq. (18) requires to model the subfilter tensorial dissipation rate $(\epsilon_{ij})_{SFS}$ defined in Eq. (24) that can be decomposed into an isotropic part $2/3\epsilon_{SFS}\delta_{ij}$ and an anisotropic part $(\epsilon_{ij})_{SFS} - 2/3\,\epsilon_{SFS}\delta_{ij}$ assumed already modeled in the redistribution term Π_{ij}. The modeling of dissipation-rate ϵ_{SFS} is made in the present case by means of its transport equation without referring to the grid information in the aim to obtain an accurate result in particular situations of non-equilibrium flows when the grid-size is no longer a good estimate of the characteristic turbulence length-scale. As a result of the theory developed in the spectral space,[3] the instantaneous modeled transport equation for the subfilter-scale dissipation-rate ϵ_{SFS} reads

$$\frac{D\epsilon_{SFS}}{Dt} = c_{SFS\epsilon_1}\frac{\epsilon_{SFS}}{k_{SFS}}P - c_{SFS\epsilon_2}\frac{\epsilon^2_{SFS}}{k_{SFS}} + J_\epsilon - 4\nu\epsilon_{ijk}\Omega_j(\epsilon_{ik})_{SFS}, \quad (39)$$

where $c_{SFS\epsilon_1}$ is a constant coefficient whereas the coefficient $c_{SFS\epsilon_2}$ appearing in Eq. (39) is now a function of the ratio to the subfilter energy to the total energy $\langle k_{SFS}\rangle/k$ as follows:[3]

$$c_{SFS\epsilon_2} = c_{\epsilon_1} + \frac{\langle k_{SFS}\rangle}{k}\left(c_{\epsilon_2} - c_{\epsilon_1}\right), \quad (40)$$

and where the coefficients c_{ϵ_1} and c_{ϵ_2} appearing in this equation denote the usual constants used in the RANS modeling. The theory[3] shows that the coefficients c_{ϵ_1} and $c_{SFS\epsilon_1}$ must take the same identical value $c_{SFS\epsilon_1} = c_{\epsilon_1}$ in the RANS limit. Equation (39) using the relation (40) constitutes the main feature of the PITM approach where only the part of the energy spectrum for $\kappa > \kappa_c$ is modeled. The ratio $\langle k_{SFS}\rangle/k$ appearing in Eq. (40) is evaluated by means of an accurate energy spectrum $E(\kappa)$ inspired from a Von Kármán like spectrum valid on the entire range of wave numbers

$$E(\kappa) = \frac{\frac{2}{3}\beta_\eta L_e^3\, k\, \kappa^2}{\left[1 + \beta_\eta(\kappa\, L_e)^3\right]^{11/9}}, \tag{41}$$

where β_η is a constant coefficient, leading to the result[4]

$$\frac{\langle k_{SFS}\rangle}{k} = [1 + \beta_\eta(\kappa_c L_e)^3]^{-2/9}. \tag{42}$$

So that $c_{SFS\epsilon_2}$ takes the analytical expression[4]

$$c_{SFS\epsilon_2}(\eta_c) = c_{\epsilon_1} + \frac{c_{\epsilon_2} - c_{\epsilon_1}}{\left[1 + \beta_\eta\, \eta_c^3\right]^{2/9}}. \tag{43}$$

Equation (43) indicates that the function $c_{SFS\epsilon_2}$ acts like a dynamic parameter which controls the spectral distribution of turbulence. Note that this model is basically different from an URANS (unsteady Reynolds averaged Navier-Stokes) approach, although it is fully compatible with it at the limit of vanishing cutoff wave number. In contrast to the RANS modeling where the whole spectrum is modeled, it is of importance to note that Eq. (39) is modeled only in the subfilter spectral interval $[\kappa_c, \infty[$. As it can be seen, the production term appearing in Eq. (39) therefore depends on the cutoff wave number. But the subfilter dissipation rate ϵ_{SFS} physically must remain unaffected by κ_c, at least for high Reynolds numbers. Indeed, one has to keep in mind that the subfilter dissipation rate can be interpreted as a spectral flux passing through the spectrum at the dissipative wave number κ_d of energy which is transferred from the large scales to the small scales.[1] The theoretical value of the coefficient β_η appearing in Eq. (43) is obtained by the limiting condition of the Kolmogorov law at high wave numbers $\lim_{\kappa\to\infty} E(\kappa) = C_K\epsilon^{2/3}\kappa^{-5/3}$ where C_K is the Kolmogorov constant leading to the theoretical value $\beta_{\eta_{th}} = [2/(3C_K)]^{9/2}$. The diffusion term J_ϵ appearing on the left-hand side of Eq. (39) is modeled assuming a well-known gradient law hypothesis

$$J_\epsilon = \frac{\partial}{\partial x_j}\left(\nu\frac{\partial \epsilon_{SFS}}{\partial x_j} + c_\epsilon\frac{k_{SFS}}{\epsilon_{SFS}}(\tau_{jm})_{SFS}\frac{\partial \epsilon_{SFS}}{\partial x_m}\right), \tag{44}$$

where the coefficient c_ϵ is a constant coefficient. Note that the last term involving the rotation appearing in the right-hand side of Eq. (39) reduces to zero if assuming local isotropy state of the tensorial dissipation-rate $(\epsilon_{ij})_{SFS} = 2/3\, \epsilon_{SFS}\delta_{ij}$.

E. Low Reynolds number formulation

The final subfilter stress model is integrated to the wall and is then complemented by low Reynolds number extensions that enable to reproduce properly the mean velocity and turbulent stresses in the wall boundary layer. To do that, a damping function f_w of the Reynolds number $R_t = k_{SFS}^2/(\nu\epsilon_{SFS})$ is introduced in the model for the near-wall correction. A new term Π_{ij}^w is also added in the original redistributive term Π_{ij} in order to account for the wall effects caused by the reflexion of the pressure fluctuations from rigid walls. This term has been found beneficial for accurately reproducing the logarithmic law of the mean velocity profile in the boundary layer. Taking into account these developments, the modeled transport equation for the subfilter scale stress in a low Reynolds number version reads

$$\frac{D(\tau_{ij})_{SFS}}{Dt} = P_{ij}^1 + P_{ij}^2 + \Pi_{ij}^1 + \Pi_{ij}^2 + \Pi_{ij}^w + J_{ij} - \frac{2}{3}\epsilon_{SFS}\delta_{ij}, \tag{45}$$

where Π_{ij}^w is defined by

$$\Pi_{ij}^w = c_w k_{SFS}\left(S_{ij} - \frac{1}{3}S_{mm}\right)(1 - f_w), \tag{46}$$

TABLE II. Functions used in the subfilter stress model.

Functions	Expressions
R_t	$k_{SFS}^2/(\nu\epsilon_{SFS})$
c_{SFS_1}	$[c_1 + \bar{c}_1(P/\epsilon)]\,h(\eta_c)$
c_{SFS_2}	$3(c_{SFS_1} - 2)$
c_1	$2. + 1.4 f_w(R_t)$
$\bar{c}_1$	$c_1^* f_w(R_t)$
c_3	$[\bar{c}_3 - c_3^* II^{1/2}]$
f_w	$1 - \exp[-(R_t/190)^4]$
h	$(1 + \alpha_{\eta 1}\,\eta_c^2)/(1 + \alpha_{\eta 2}\,\eta_c^2)$
Δ	$\Delta = \Delta_a\left(\zeta + (1-\zeta)\frac{\Delta_b}{\Delta_a}\right)$
η_c	$(\pi\, k^{3/2})/[\Delta\ (\epsilon_{SFS} + \epsilon^<)]$
$c_{SFS\epsilon_2}$	$c_{\epsilon_1} + [(c_{\epsilon_2} - c_{\epsilon_1})/\left(1 + \beta_\eta\,\eta_c^3\right)^{2/9}]$

and c_w is a constant coefficient. The damping function f_w introduced in Eq. (46) satisfies the limiting conditions $lim_{\ R_t\to 0}\ f_w(R_t) = 0$ and $lim_{\ R_t\to\infty}\ f_w(R_t) = 1$ implying that $lim_{\ R_t\to\infty}\ \Pi_{ij}^w(R_t) = 0$ for not altering the model at high Reynolds number. The recommended function and constant coefficients used in Eq. (45) have been obtained in the present case by a tedious work of systematic tuning and they are listed in Tables II and III. The present function c_{SFS_1} involved in the slow redistribution term satisfies the following constraint $lim_{\ R_t\to 0}\ c_{SFS_1}(R_t) = 2$ and is therefore consistent with the two-component limit turbulence states implying that the flatness parameter defined by $A = 1 - 9(II/2 - III)$ where $II = a_{ij}a_{ji}$ and $III = a_{ij}a_{jk}a_{ki}$ denote the second and third invariants, respectively, goes to zero at the walls, e.g., $lim_{\ R_t\to 0}\ A(R_t) = 0$.[65] The function c_3 verifies the limiting condition $lim_{\ R_t\to 0}\ c_3(R_t) = 0$. The value of the constant coefficient $\bar{c}_3$ is set to 0.8 for satisfying the consistency with the rapid distortion theory for homogeneous strained turbulence in an initially isotropic state.[66] The constant coefficient c_s used in the diffusion term J_{ij} takes on the value 0.22. The modeled transport equation for the subfilter dissipation rate ϵ_{SFS} Eq. (39) is also developed in a low Reynolds number formulation for approaching walls as follows:

$$\frac{D\epsilon_{SFS}}{Dt} = c_{SFS\epsilon_1}\frac{\epsilon_{SFS}}{k_{SFS}}P - c_{SFS\epsilon_2}\frac{\epsilon_{SFS}\tilde{\epsilon}_{SFS}}{k_{SFS}} + J_\epsilon, \tag{47}$$

where $\tilde{\epsilon}_{SFS} = \epsilon_{SFS} - 2\nu(\partial\sqrt{k_{SFS}}/\partial x_n)^2$, x_n being the normal coordinate to the wall. The quantity $\tilde{\epsilon}_{SFS}$ is introduced in Eq. (47) to prevent the destruction term to go to infinity as the wall is approached. The values used in the original SSG model[5] are $c_{\epsilon_1} = 1.44$ and $c_{\epsilon_2} = 1.83$. In the present case, the values retained are $c_{SFS\epsilon_1} = c_{\epsilon_1} = 1.5$ and $c_{\epsilon_2} = 1.9$, so that the difference $c_{\epsilon_2} - c_{\epsilon_1}$ approximately remains the same. Moreover, for each set of coefficients, the ratio $\alpha = (c_{\epsilon_2} - 1)/(c_{\epsilon_1} - 1)$ which is the key parameter for homogeneous rotating flows[67] takes on close values, 1.80 and 1.88, respectively. The diffusion coefficient c_ϵ is set to 0.18. The coefficient β_η appearing in Eq. (43) is optimized to $\beta_\eta = [2/(3C_K)]^{9/2} \approx 0.0355$ corresponding to the Kolmogorov value $C_K = 1.4$.[4,45] The coefficients used in the function h are $\alpha_{\eta 1} = 1.3/400$ and $\alpha_{\eta 2} = 1/400$, respectively. The empirical coefficient ζ is set to 0.8 for taking into account the anisotropy of the grids. The functions and coefficients used in Eq. (47) are listed in Table III. If the c_{SFS_2} term may cause numerical difficulties, it can be suppressed. From a practical point of view, the homogeneous SSG model is recovered for $\eta_c \to 0$ and $R_t \to \infty$. As a result, one can finally remark that the present turbulence model takes a basic

TABLE III. Constants coefficients used in the pressure-strain term Π_{ij}.

Coefficients	c_1^*	$\bar{c}_3$	c_3^*	c_4	c_5	c_w
	1.8	0.8	1.30	1.25	0.4	0.185

formulation that embodies some advanced concepts of second-moment closures. It contains only a few empirical terms acting at low Reynolds number.

IV. NUMERICAL METHOD AND CONDITIONS OF COMPUTATIONS

A. Numerical method

The numerical simulations are performed by using the research code developed by Chaouat.[68–70] The governing equations of motion as well as the transport equations for the subfilter scale stresses and dissipation-rate are integrated in time by an explicit Runge-Kutta scheme of fourth-order accuracy. The convective fluxes are computed by a quasi-centered scheme of second-order accuracy in space. The code has been successfully calibrated on basic test cases such as the decay of homogeneous isotropic turbulence and the fully turbulent channel flows.[4,71] In practice, it must be pointed out that the present simulations solving all the transport equations require only 30% more CPU time than conventional LES simulations using eddy viscosity models. This is due to the basic form of the transport equations which is well appropriate to vectorization and parallelization techniques.[1,70] As shown in Table IV referring to engineering applications,[1,2,45,47] several flows have been simulated in the past using the PITM and DSM models on different grids. For the PITM method requiring to solve seven transport equations for $(\tau_{11})_{SFS}$, $(\tau_{12})_{SFS}$, $(\tau_{13})_{SFS}$, $(\tau_{22})_{SFS}$, $(\tau_{23})_{SFS}$, $(\tau_{33})_{SFS}$, and ϵ_{SFS}, the higher cost is in fact highly compensated by the possibility of coarsening the mesh. So that the PITM method allows a drastic reduction of the computational cost.

B. Practical convergence enhancement

As shown in Sec. III, the coefficient $c_{SFS\epsilon_2}$ defined in Eq. (43) involving the ratio $\langle k_{SFS}\rangle/k$ constitutes the key parameter of the PITM method. This coefficient induces a strong coupling interaction between the subfilter-scale stress transport Eq. (18), the subfilter dissipation-rate Eq. (39), and the filtered momentum Eq. (5) and it controls the behavior of the PITM method. At each temporal iteration, the model works to bring the calculated $\langle k_{SFS}\rangle/k$ value close to the equilibrium value, solution of Eq. (42) deduced from the theoretical Von Kármán energy spectrum $E(\kappa)$ given by Eq. (41). The equality is exactly reached only in strict equilibrium flows. The mechanism in the ϵ equation can be viewed as a "return to equilibrium"process. In practice, with the aim to avoid the model to reach a purely RANS or LES limiting behavior during the transition phase and also to accelerate the numerical convergence towards the solution in the permanent state, a procedure[49] which locally consists of modifying the coefficient $c_{SFS\epsilon_2}$ to force the model to approach more rapidly the expected energy ratio has been activated during the computations. The equilibrium energy ratio $r_{eq} = \langle k_{SFS}\rangle/k$ given by Eq. (42) is then compared with the ratio value r_{CFD} computed by the simulation. The dynamic correction of the subfilter coefficient $\delta c_{SFS\epsilon_2}$ is calculated by means of the parameter r_{CFD}/r_{eq} as follows:

$$\delta c_{SFS\epsilon_2} = \chi\, c_{SFS\epsilon_2}\left(1 - \frac{r_{CFD}}{r_{eq}}\right), \tag{48}$$

where χ is a constant parameter set to 0.1. This correction allows to adjust the coefficient $c_{SFS\epsilon_2}$ to get a closer estimate of the ratio $r_{CFD} = \langle k_{SFS}\rangle/k$. This procedure is applied during the transition phase of the PITM simulations.

TABLE IV. Simulations of flows using DSM and PITM models.

Engineering applications	Authors	Turbulence model	Grid points
Channel flows with wall injection	Apte and Yang;[72]	DSM	8.96×10^6
	Chaouat and Schiestel[1]	PITM	1.4×10^6
Channel flows with periodic hills	Breuer *at al.*[73]	DSM	13.1×10^6
	Chaouat[45]	PITM	2.4×10^5

C. Conditions of computations

The computational domain is of dimension $3\delta \times 2\delta \times \delta$ in the streamwise, spanwise, and normal directions, respectively, x_1, x_2, x_3 and the rotation vector is oriented along the spanwise direction as seen by Figure 1. The box size is sufficiently large for ensuring the vanishing of two-point correlation functions in the streamwise direction. All the present simulations are performed on a coarse grid $24 \times 48 \times 64$ and on a medium grid $84 \times 64 \times 64$ for assessing the performances of the subfilter scale stress model and for checking the grid independence of solutions when the filter with is changed. In the present case, the grid-points are distributed with non-uniform spacing taking into account a refinement near the wall. The simulations are performed at the Reynolds number $R_\tau = u_\tau \delta / 2\nu = 386$ based on the friction velocity u_τ and the channel half width $\delta/2$. A constant pressure gradient term $G = 2\rho_\tau u_\tau^2/\delta$ has been added in the motion equation to balance the friction at the walls. For the coarse and medium grids, the first grid point in the direction normal to the wall is located at the dimensionless distance $\Delta_3^+ = \Delta_3\, u_\tau/\nu = 1.0$. In the two remaining directions, the grid spacing are of constant values. More precisely, the grid spacing Δ_i^+ is computed by the relation $\Delta_i^+ = \Delta_i u_\tau/\nu = 2L_i R_\tau/(N_i\delta)$ where L_i and N_i denote the length of the computational box in the ith direction and the number of grid points, respectively. For the coarse grid, one can obtain easily $\Delta_1^+ \approx 96.5$ and $\Delta_2^+ \approx 32.2$ whereas for the medium grid, $\Delta_1^+ \approx 27.5$ and $\Delta_2^+ \approx 24.1$. These values are strongly less stringent than the recommendations for wall-resolved LES.[74] As a consequence, the PITM simulations does not require extremely large memory and computing time resource.

V. NON-ROTATING CHANNEL FLOWS

A. Computational framework

The PITM and Smagorinsky[75] simulations are performed on the very coarse grid at the Reynolds number $R_\tau = 386$ or, equivalently, at the Reynolds number $R_m = u_m\delta/\nu \approx 14\,000$ based on the bulk velocity u_m.

B. Mean velocity

The velocities and stresses are compared with data of direct numerical simulations[76] as well as highly resolved large eddy simulations.[6] As a result, Figure 2 shows the profiles of the statistical mean velocity $\langle u_1\rangle/u_\tau$ in logarithmic coordinates $x_3^+ = x_3 u_\tau/\nu$ for both the PITM and Smagorinsky simulations. It is found that the mean velocity predicted by the PITM agrees very well with the DNS data. This result was expected since the velocity profile is mainly governed by the model that behaves like the statistical Reynolds stress model (RSM) in the wall region, as it will be seen in the following. This result demonstrates that the formulation of the low Reynolds number turbulent model presented in Sec. III is well appropriate for accurately reproducing the boundary layer. In the contrast to the PITM velocities, the Smagorinsky velocities strongly deviate from the DNS data because of the mismatch that occurs in the logarithmic region. The mean velocity is overpredicted by about 50% with respect to the DNS data.

C. Turbulent shear stress

Figure 3 displays the mean shear stress τ_{13}/u_τ^2 as well as the subfilter and resolved stresses $\langle(\tau_{13})_{SFS}\rangle/u_\tau^2$ and $\langle(\tau_{13})_{LES}\rangle/u_\tau^2$, respectively, for both simulations. The mean shear stress is computed as the sum of the subfilter and resolved stresses. One can see that the mean shear stress returned by the PITM simulation presents an excellent agreement with the DNS data and that the one provided by the SM simulation also agrees relatively well with the DNS. A better result is however obtained by the PITM because the shear stress is directly computed by its transport equation whereas it is evaluated by the Boussinesq hypothesis for the Smagorinsky model. For both simulations, the agreement with the DNS data results from the balance between the mean pressure gradient in the streamwise direction and the mean shear stress gradient in the normal direction to the walls. It is of interest to

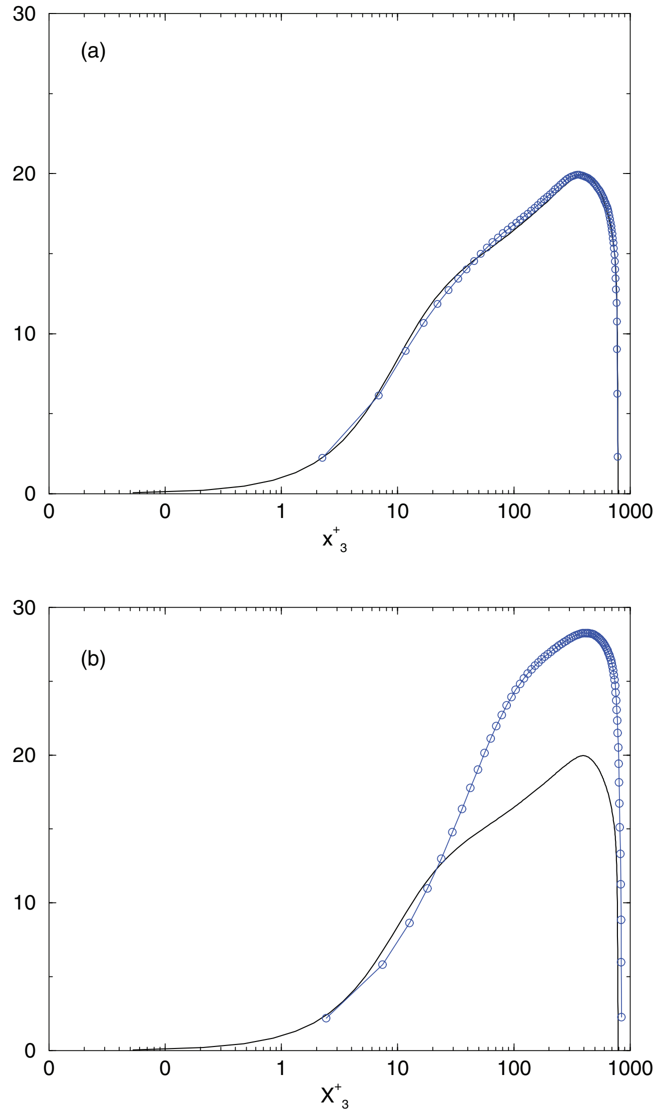

FIG. 2. Mean velocity profile $\langle u_1 \rangle / u_\tau$ in logarithmic coordinate. (a) PITM1 (24 × 48 × 64) ◦. (b) SM (24 × 48 × 64) ◦. DNS:[76] —. $R_\tau = 395$; $R_m \approx 14\,000$.

analyze the sharing out of turbulence energy among the modeled and resolved turbulence scales. From Figure 3, the evidence is clear that the modeled stress is of higher intensity than the resolved stress in the near wall region whereas the reverse situation occurs in the center of the channel. This outcome was also obtained by Fadai-Ghotbi *et al.*[48,49] when performing numerical simulations of turbulent channels flows on coarse, medium, and refined grids using the TPITM method. For the PITM simulation, this results was partially expected because the model behavior is governed by the $c_{SFS\epsilon_2}$ dynamic parameter which depends on the parameter $\eta_c = \kappa_c L_e$, interpreted as the ratio of the turbulent length-scale to the grid-size $\pi L_e/\Delta$. Near the walls, the parameter η_c goes to zero because the turbulent length-scale reduces to zero while it reaches high values in the core flow. So that this result means that the subfilter model behaves more or less like a RANS model in the near wall region and LES in the core flow. For the SM simulation, the present distribution between the modeled and resolved parts of energy simply means that the core flow is dominated by the large-scales.

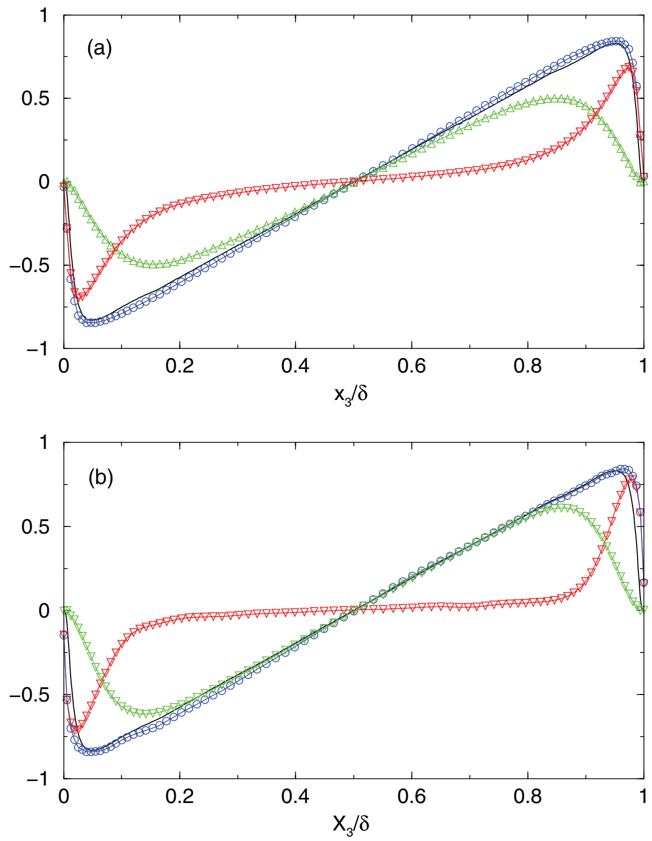

FIG. 3. Turbulent shear stress τ_{13}/u_τ^2 (a) PITM1 (24 × 48 × 64). (b) SM (24 × 48 × 64). τ_{13}/u_τ^2: ○; $\langle(\tau_{13})_{SFS}\rangle/u_m^2$: ∇; $\langle(\tau_{13})_{LES}\rangle/u_m^2$: △; DNS:[76] —. $R_\tau = 395$; $R_m \approx 14\,000$.

D. Turbulent normal stresses

Figure 4 shows the normal turbulent Reynolds stresses $\tau_{ii}^{1/2}/u_\tau$ computed as the sum of the subfilter stresses $\langle(\tau_{ii})_{SFS}\rangle^{1/2}/u_\tau$ and the resolved stresses $\langle(\tau_{ii})_{LES}\rangle^{1/2}/u_\tau$ for the PITM simulation as well as the resolved stresses for the SM simulation. One has to keep in mind that for the PITM simulation, the normal subfilter stresses are solution of the system (18) of transport equations. But for the SM simulation using the Boussinesq hypothesis assuming a linkage between the stress and strain components, there is no means at all of computing the normal turbulent stresses. It can be pointed out that only transport turbulent models including at least one transport equation for a turbulent quantity, usually the subgrid turbulent energy, can provide the normal subgrid stresses. As a result, the PITM stresses present a relatively good agreement with the DNS data although the intensity of the turbulent stresses is slightly overpredicted in the channel. The turbulent peaks near the walls are well captured by the PITM simulation but not their rapid drops reproduced by the DNS data. As previously found for PITM channel flow simulations,[1,4] this slight remaining discrepancy with the DNS data mainly results from the numerical scheme diffusion effects attributed to the mesh discretization errors. As expected, better agreements with DNS are obtained for refined grids.[1,4] On the other hand, the SM simulation returns resolved turbulent stresses which highly disagree with the DNS data. The streamwise stress is highly overpredicted everywhere in the channel whereas the spanwise and normal stresses are underpredicted. The discrepancies with the reference data are in fact greater than those observed in this figure because the modeled energy has not be taken into account in the computation. This disagreement with the data must be attributed to the very coarse grid resolution. Indeed, because of its simple formulation based on equilibrium assumptions, the Smagorinsky model requires very refined grids for providing accurate results. These present results indicate that

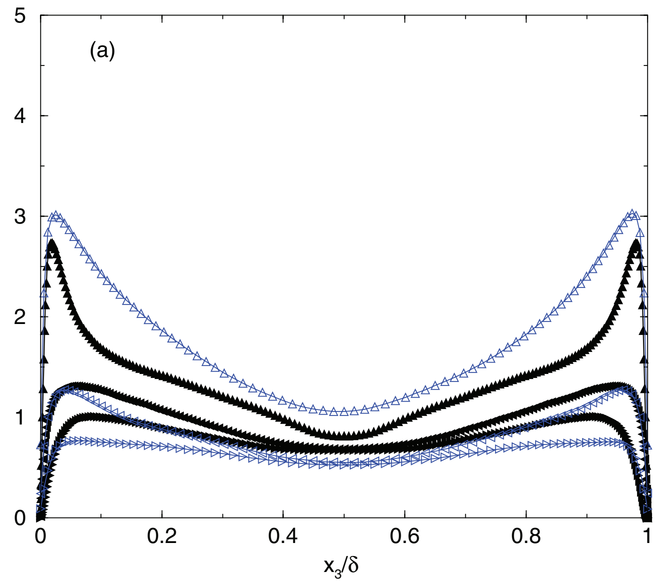

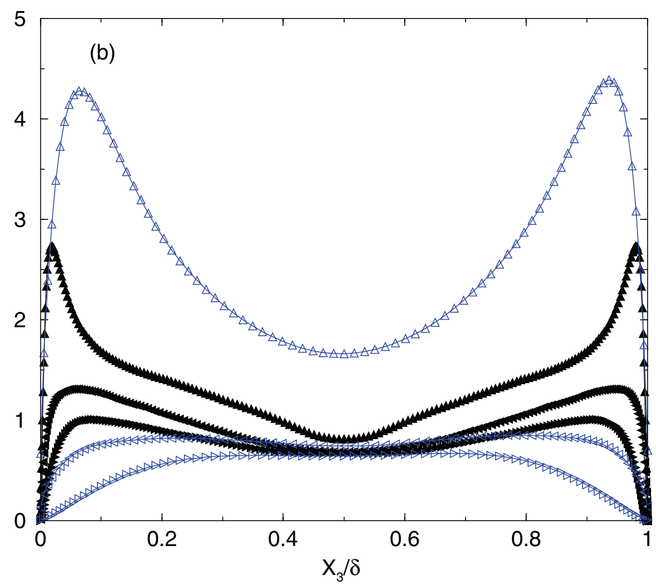

FIG. 4. Turbulent Reynolds stresses $\tau_{ii}^{1/2}/u_\tau$ (a) PITM1 (24 × 48 × 64) △: i = 1; ◁: i=2; ▷: i = 3. (b) SM (24 × 48 × 64) △: i = 1; ◁: i = 2; ▷: i = 3. DNS:[76] ▲: i = 1, ◀: i = 2, ▶: i = 3. DNS:[76] ▲: i = 1, ◀: i = 2, ▶: i = 3. $R_\tau = 395$; $R_m \approx 14\,000$.

SM computations are not able to reproduce correctly turbulent flows performed on coarse grids. Relatively to viscosity-based subgrid models, this study demonstrates the advantages of applying the present sufbilter stress model developed in the framework of second-moment closures.

VI. ROTATING CHANNEL FLOWS

A. Computational framework

Considering these results, it is not worth simulating rotating channel flows on such coarse grids by using the Smagorinsky model, the rotating channel flows being of much more complex physics than non-rotating channel flows. Consequently, only PITM simulations are processed in the following. In this work, the turbulent rotating flows are simulated at the Reynolds number

$R_\tau = 386$ corresponding to the bulk Reynolds number $R_m \approx 14\,000$ at different values of the rotation number $R_o = \Omega\delta/u_m$ varying from moderate, medium, and very high rotation rates $R_o = 0.17$, 0.50, and 1.50 on the coarse and medium grids. This choice is motivated by the study of the consistency of the subfilter model when the filter width is changed. In addition, the rotating channel flow is also performed on the refined grid $124 \times 84 \times 84$ at $R_o = 1.50$ to prove in practice that the PITM method reverts to standard highly resolved LES as the grid-size decreases. Note that in the literature, rotating flows are sometimes characterized by the Rossby number defined by $Rg_m = 3u_m/\delta\Omega$ which is directly related to the rotation number by $Rg_m = 3/R_o$. As shown in Figure 1, the vector rotation is along the spanwise direction x_2. The PITM results including the velocities and stresses are compared with the data of highly resolved LES simulation performed by Lamballais *et al.*[6,18] using the spectral-dynamic model derived from the eddy-damped quasi normal Markovian statistical theory.[24,77]

B. Mean velocity

Figures 5–7 show the mean dimensionless velocity profiles normalized by the bulk velocity $\langle u_1\rangle/u_m$ versus the global coordinates for both rotation regimes and for each grid. Because of the rotation effects, one can see that the mean velocity presents an asymmetric character which is more

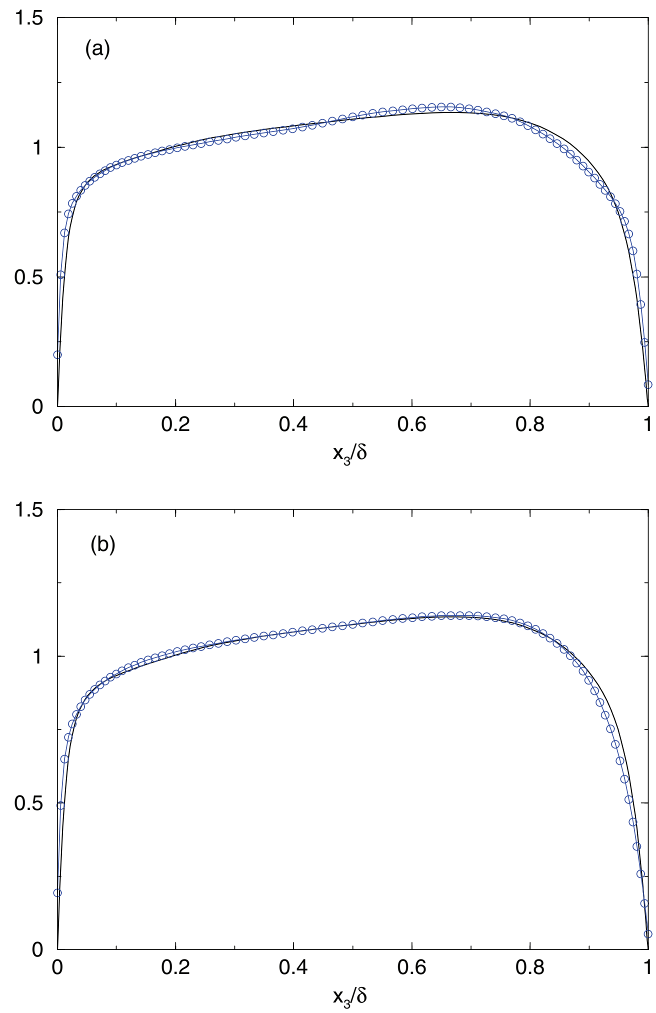

FIG. 5. Mean velocity profile $\langle u_1\rangle/u_m$ in global coordinate. (a) PITM1 ($24 \times 48 \times 64$): ○; (b) PITM2 ($84 \times 64 \times 64$): ○; Highly resolved LES:[6] —. $R_m = 14\,000$, $R_o = 0.17$.

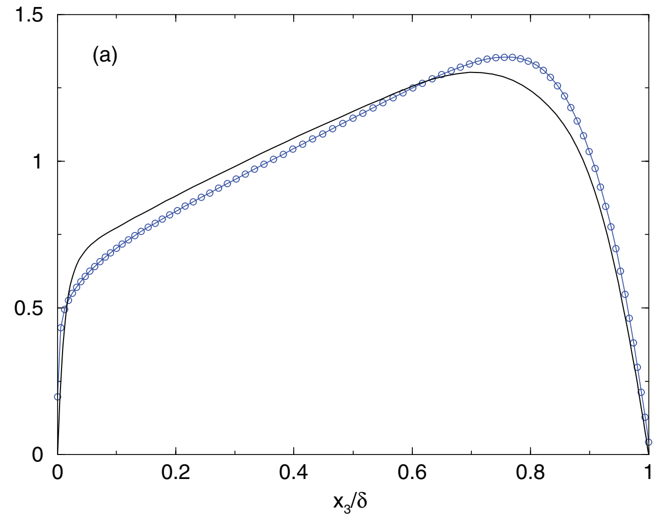

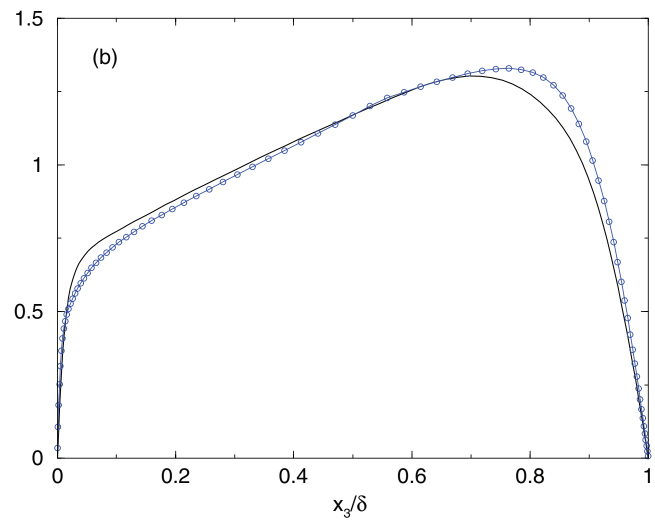

FIG. 6. Mean velocity profile $\langle u_1 \rangle / u_m$ in global coordinate. (a) PITM1 ($24 \times 48 \times 64$): $\circ$; (b) PITM2 ($84 \times 64 \times 64$): $\circ$; Highly resolved LES:[6] —. $R_m = 14\,000$, $R_o = 0.50$.

and more pronounced as the rotation rate increases from $R_o = 0.17$ to 1.50. At high rotation rate, one can observe that the mean velocity profile is very close to a parabolic shape corresponding to the laminar Poiseuille profile in the cyclonic wall region. Overall, one can see that both PITM simulations provide mean velocity profiles that agree very well with the reference data,[6] even for the PITM1 simulation performed on the coarse grid. For both simulations performed at $R_o = 0.17$, 0.50, and 1.50, one can notice that the mean velocity profile exhibits a linear region of constant shear stress in the nearly whole channel although this is less marked at the lower rotation rate $R_o = 0.17$. More precisely, the computation indicates that the slope of the mean velocity gradient $\partial \langle u_1 \rangle / \partial x_3$ is approximately equal to $2\Omega_2$, and corresponds to a nearly-zero mean spanwise absolute vorticity vector, i.e., $\langle W_2 \rangle = \langle \omega_2 \rangle + 2\Omega_2 \approx 0$ where $\omega_i = \epsilon_{ijk} \partial u_k / \partial x_j$ represents the vorticity vector, as already noticed experimentally by Johnston et *al*.[8] By considering the Richardson number defined as

$$R_i = \frac{-\Omega_2(\langle S_{13} \rangle - \Omega_2)}{\langle S_{13} \rangle^2}, \tag{49}$$

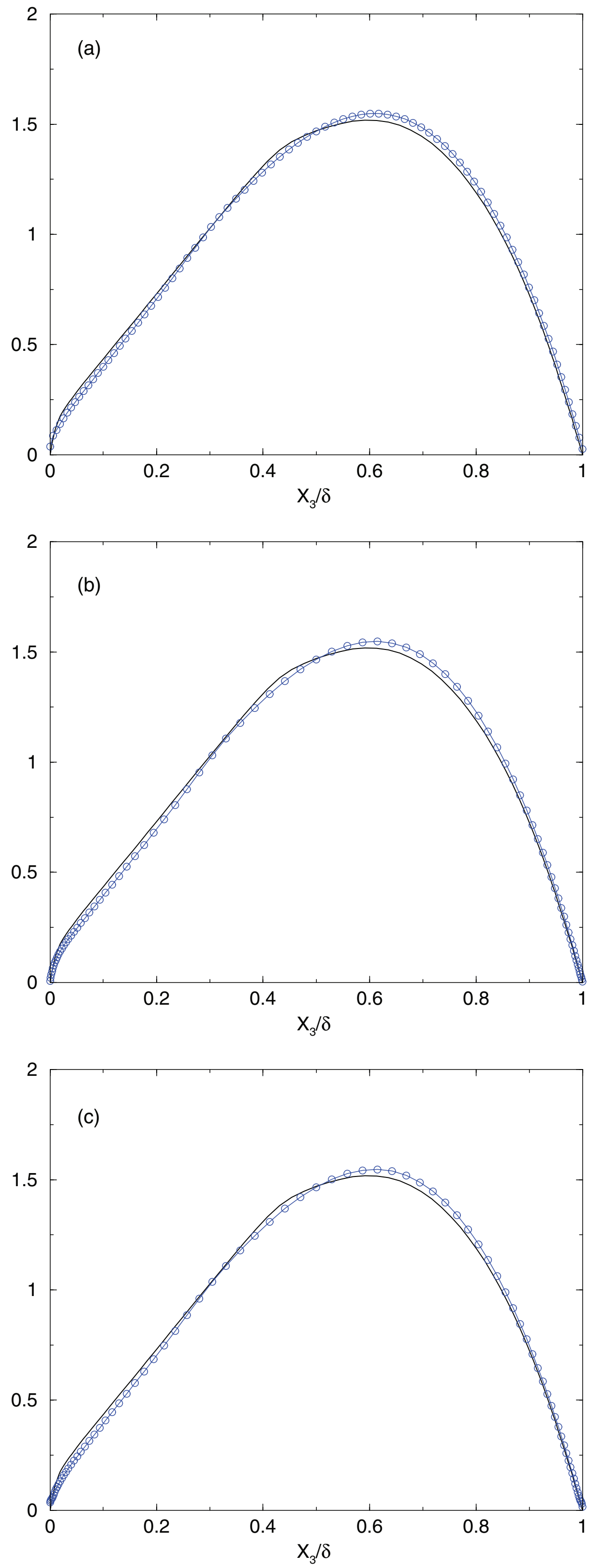

FIG. 7. Mean velocity profile $\langle u_1 \rangle / u_m$ in global coordinate. (a) PITM1 (24 × 48 × 64): ○; (b) PITM2 (84 × 64 × 64): ○; (c) PITM3 (124 × 84 × 84): ○; Highly resolved LES:[6] —. $R_m = 14\,000$, $R_o = 1.50$.

it simple matter to show that this particular portion of the profile represents in fact a region of neutral stability $R_i \approx 0$. On the cyclonic side, the rotation stabilizes the flow whereas on the anticyclonic side, it destabilizes the flow because the Richardson number R_i is either positive or negative.[78]

C. Turbulent shear stress

Figures 8–10 display the subfilter, resolved, and total turbulent shear stresses denoted $\langle(\tau_{13})_{SFS}\rangle/u_\tau^2$, $\langle(\tau_{13})_{LES}\rangle/u_\tau^2$, and τ_{13}/u_τ^2 for the PITM simulations performed at each rotation rate. As shown in Sec. V concerning the non-rotating case, these figures clearly indicate that the subfilter stress model behaves more or less like the RANS/RSM model in the near wall region, although the grid is very refined in the normal direction to the wall, and like LES in the core flow. One can observe that the distribution of the turbulent shear stress energy between the modeled and resolved parts is modified according to the location of the cutoff wave number which varies versus the grid size of the mesh, but the total shear stress energy remains almost the same and agrees relatively well with the reference data of the highly resolved LES. More precisely, the SFS part of the shear stress associated to the coarse grid appears larger than the one observed for the medium grid whereas the reverse situation occurs for the resolved part of the shear stress. The case performed at the rotation rate $R_o = 1.50$ deserves a particular attention since the shear stress vanishes in the cyclonic region which roughly extends from the half channel-width to the upper wall, confirming that the turbulence activity dramatically decreases to zero. Only, a turbulent peak is visible in the vicinity of the anticyclonic region. As expected, the PITM3 simulation performed on the refined grid returns a quasi-zero SFS part of the shear stress so that the turbulent contribution is nearly entirely

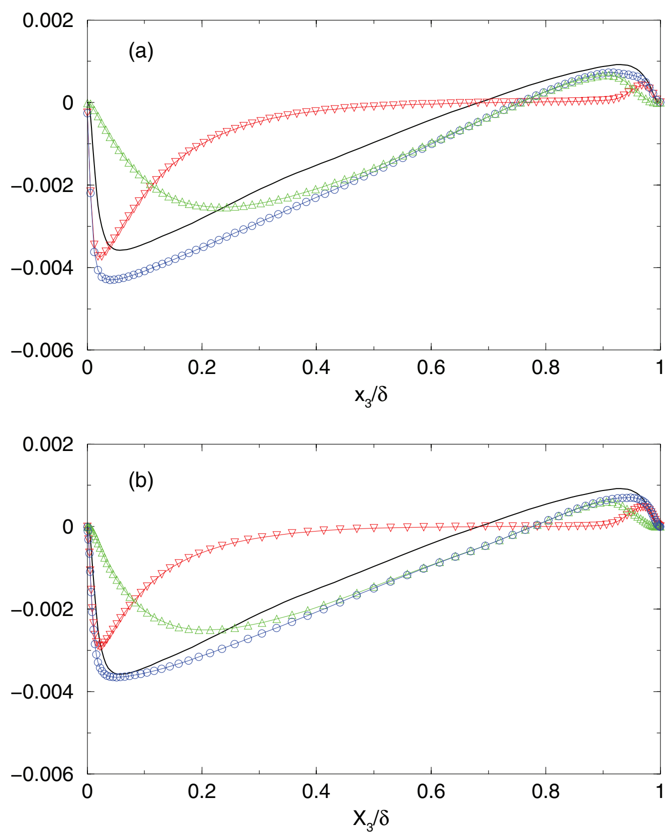

FIG. 8. Turbulent shear stress τ_{13}/u_m^2. (a) PITM1 (24 × 48 × 64); (b) PITM2 (84 × 64 × 64); τ_{13}/u_m^2: ○; $(\langle(\tau_{13})_{SFS}\rangle/u_m^2$: ∇; $(\langle(\tau_{13})_{LES}\rangle/u_m^2$: △; Highly resolved LES:[6] — . $R_m = 14\,000$, $R_o = 0.17$.

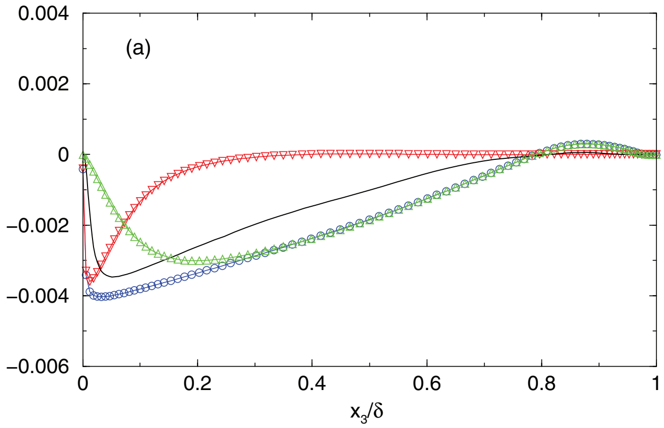

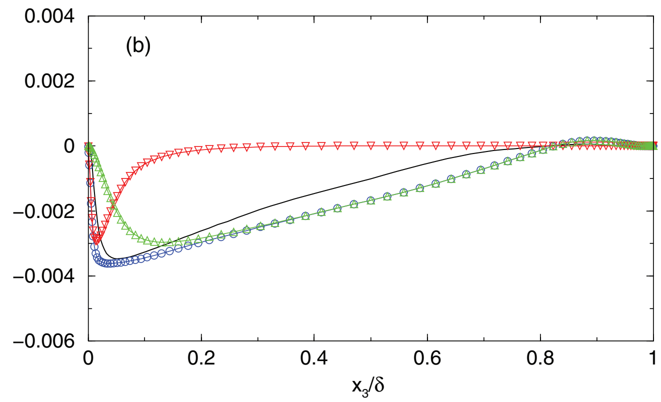

FIG. 9. Turbulent shear stress τ_{13}/u_m^2. (a) PITM1 (24 × 48 × 64); (b) PITM2 (84 × 64 × 64); τ_{13}/u_m^2: ○; $\langle(\tau_{13})_{SFS}\rangle/u_m^2$: ∇; $\langle(\tau_{13})_{LES}\rangle/u_m^2$: △; Highly resolved LES:[6] — . $R_m = 14\,000$, $R_o = 0.50$.

given by the resolved part. This result is not at all surprising since the PITM3 simulation goes to highly resolved LES.

D. Turbulent normal stresses

Figures 11–13 show the streamwise, spanwise, and normal turbulent stresses, $\tau_{11}^{1/2}/u_\tau$, $\tau_{22}^{1/2}/u_\tau$, and $\tau_{33}^{1/2}/u_\tau$ for both PITM simulations performed at the rotation rates $R_o = 0.17$, 0.50, and 1.50. The distribution of the turbulence appreciably differs between the non-rotating and rotating cases, the flow anisotropy being strongly modified. When the rotation rate is increased, the turbulence activity of the flow decreases in the whole channel but the decrease is more pronounced in the cyclonic wall region than in the anticyclonic wall region. More precisely, the intensity of the streamwise stress τ_{11} near the anticyclonic side decreases whereas the intensities of the spanwise and normal stresses τ_{22} and τ_{33} increase in the channel. This result suggests that the turbulence evolving in the cyclonic region originates from flow interactions acting in the anticyclonic region. For each stress profile plotted in Figures 11–13, a relatively good agreement is observed between the PITM and reference data, even if the PITM2 simulation returns better results than the PITM1 simulation because of the grid refinement in the streamwise and spanwise directions allowing a better flow resolution. At the highest rotation rate $R_o = 1.50$, the agreement with the data is, however, less encouraging because of the discrepancies which appear in the anticyclonic wall region. As expected, the PITM3 simulation returns very good results. Overall, the mean features of the rotating flows are well recovered by the PITM simulations with a sufficient fidelity from an engineering point of view, in particular, the decrease of the turbulence activity as the rotation rate increases and the strong modification of the

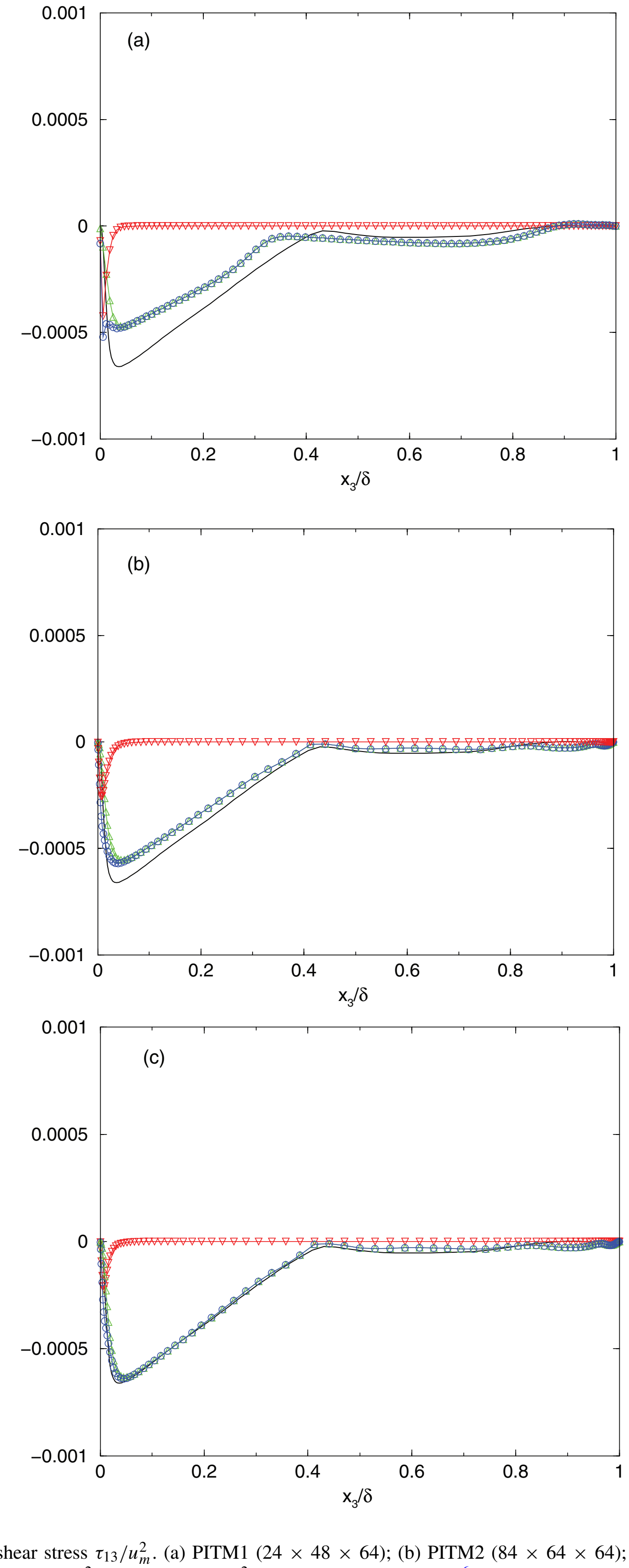

FIG. 10. Turbulent shear stress τ_{13}/u_m^2. (a) PITM1 (24 × 48 × 64); (b) PITM2 (84 × 64 × 64); (c) PITM3 (124 × 84 × 84); τ_{13}/u_m^2: ○; $\langle(\tau_{13})_{SFS}\rangle/u_m^2$: ∇; $\langle(\tau_{13})_{LES}\rangle/u_m^2$: △; Highly resolved LES:[6] — . $R_m = 14\,000$, $R_o = 1.50$.

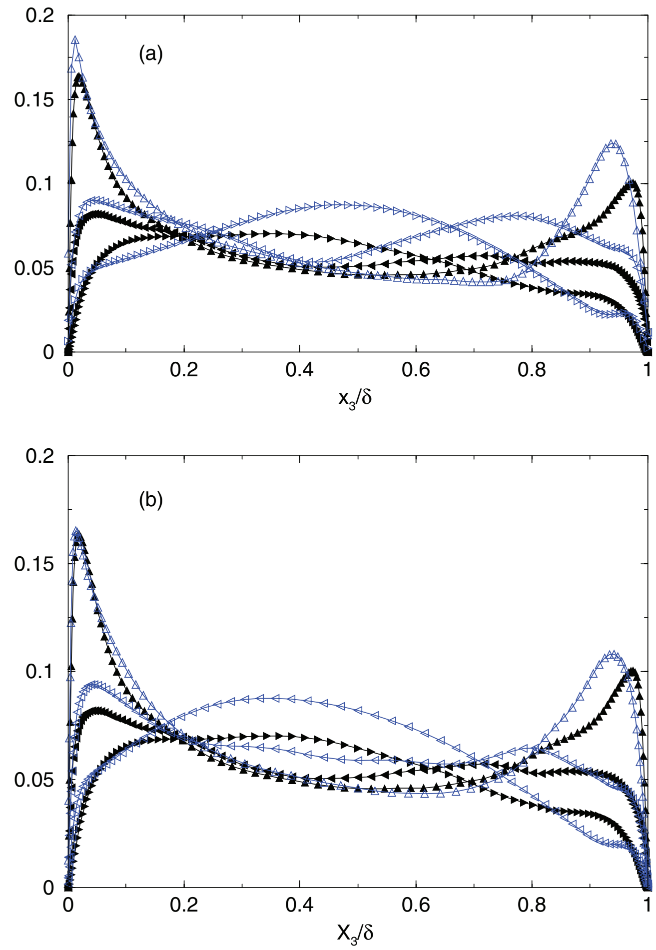

FIG. 11. Turbulent Reynolds stresses $\tau_{ii}^{1/2}/u_m$. (a) PITM1 (24 × 48 × 64); (b) PITM2 (84 × 64 × 64); △: i = 1; ◁: i = 2; ▷: i = 3. Highly resolved LES:[6] ▲: $i = 1$, ◀: $i = 2$, ▶: $i = 3$. $R_m = 14000$, $R_o = 0.17$.

flow anisotropy. In the present case, the subfilter stress model is able to reproduce the flow anisotropy on such coarse grids because of the pressure-strain correlation term that redistributes the turbulent energy among the different stress components. As it was emphasized, this term appearing only in second-moment closures is essential and demonstrates the usefulness of the present sufbilter stress model.

E. Sharing out of the turbulent energy

As shown in the Sec. III D, the subfilter stress model is mainly governed by the function $c_{SFS\epsilon_2}(\eta_c)$ that acts like a dynamic parameter which controls the spectral distribution. So that it is worth analyzing the sharing out of the turbulent energy among the subfilter and resolved turbulence scales for rotating flows. Figure 14 shows the ratio of the subfilter energy to the total energy at different rotation rates $R_o = 0.17$, 0.50, and 1.50 computed by the Von Kármán spectrum $E(\kappa)$ and the PITM1 simulations, respectively.

At the moderate rotation rate $R_o = 0.17$, one can see that the values of the equilibrium and computed ratios $\langle k_{SFS}\rangle/k$ are very close to each other and that the model behaves more or less like the RANS model in the wall regions although the grid is very refined in the normal direction and like LES in the core flow where roughly 80% of energy is simulated whereas 20% is modeled. When

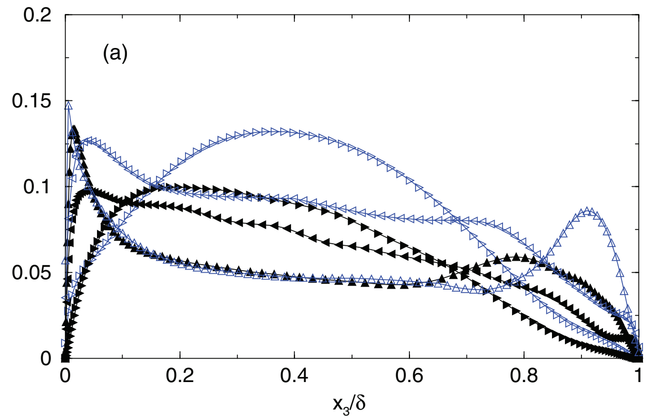

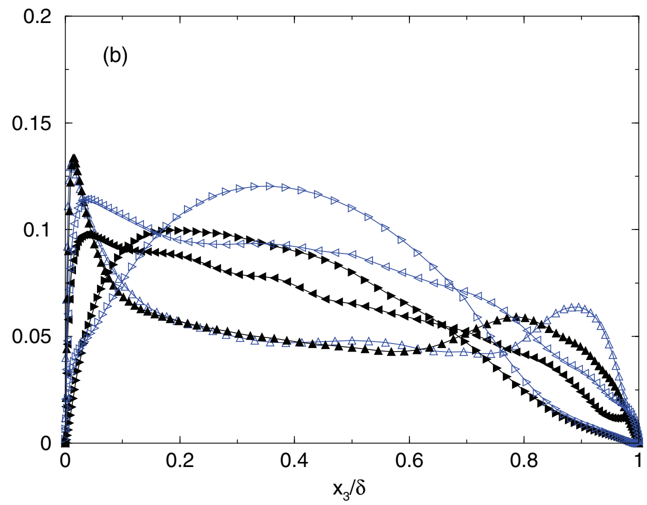

FIG. 12. Turbulent Reynolds stresses $\tau_{ii}^{1/2}/u_m$. (a) PITM1 (24 × 48 × 64); (b) PITM2 (84 × 64 × 64); △: i = 1; ◁: i = 2; ▷: i = 3. Highly resolved LES:[6] ▲: $i = 1$, ◀: $i = 2$, ▶: $i = 3$. $R_m = 14\,000$, $R_o = 0.50$.

comparing Figures 14(a)–14(c) at a given station in the channel for different rotation rates, one can observe that the ratio of the modeled energy to the total energy progressively decreases. Relatively to the total turbulence energy which decreases itself as the rotation intensifies, this result means that the modeled energy decreases more rapidly than the resolved energy implying that the subfilter model is less and less active. This rotation effect is particularly marked in the cyclonic wall region due to the fact that the computed ratio $\langle k_{SFS}\rangle/k$ of the PITM1 simulation at $R_o = 1.50$ dramatically reduces to zero. In this region, the value of the computed ratio $r_{CFD} = \langle k_{SFS}\rangle/k$ strongly differs from the equilibrium ratio value r_{eq} suggesting that the flow departs from the spectral equilibrium. Different reasons can explain this outcome. The recent simulations of Grundestam *et al.*[20] and Brethouwer *et al.*[21] have revealed the presence of large streamwise vortices evolving in time and space in the channel. As a result, these authors put in evidence the presence of quasi-periodic instabilities corresponding to intense bursting events in the cyclonic wall region of the flow at $R_o = 1.3$ and 1.5. These findings clearly show that rotating flows at high rotation rates are out of spectral equilibrium and that the cascading process must be consequently modified in comparison with the equilibrium one. In this case, it is not surprising if the ratio values r_{eq} and r_{CFD} differ from each other. This result only means that the model is able to take into account situations of non-equilibrium flows although the mechanism formulated in the dissipation-rate equation traduces the return to equilibrium. As the rotation rate increases, another point to mention relates to the profiles of the ratio $\langle k_{SFS}\rangle/k$ which become more and more asymmetric with respect to the channel center. So that, the dissipation-rate

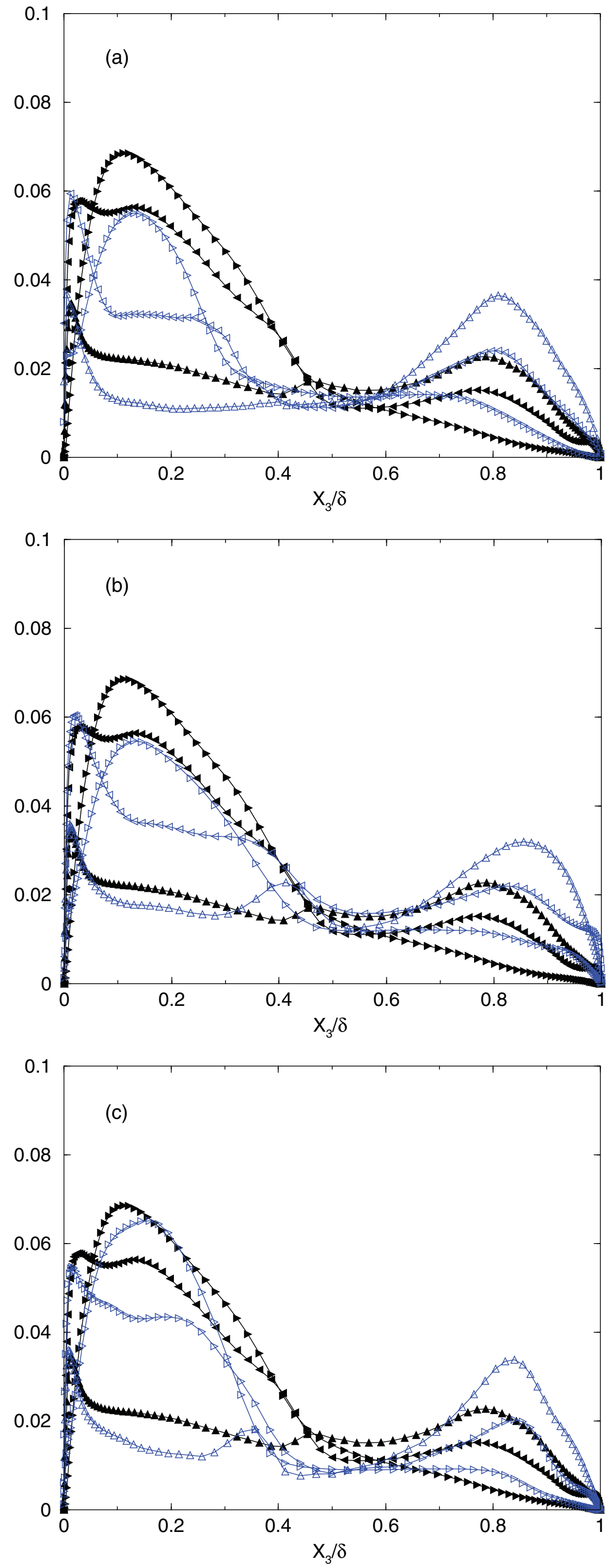

FIG. 13. Turbulent Reynolds stresses $\tau_{ii}^{1/2}/u_m$. (a) PITM1 (24 × 48 × 64); (b) PITM2 (84 × 64 × 64); (c) PITM3 (124 × 84 × 84); △: i = 1; ◁: i = 2; ▷: i = 3. Highly resolved LES:[6] ▲: $i = 1$, ◀: $i = 2$, ▶: $i = 3$. $R_m = 14000$, $R_o = 1.50$.

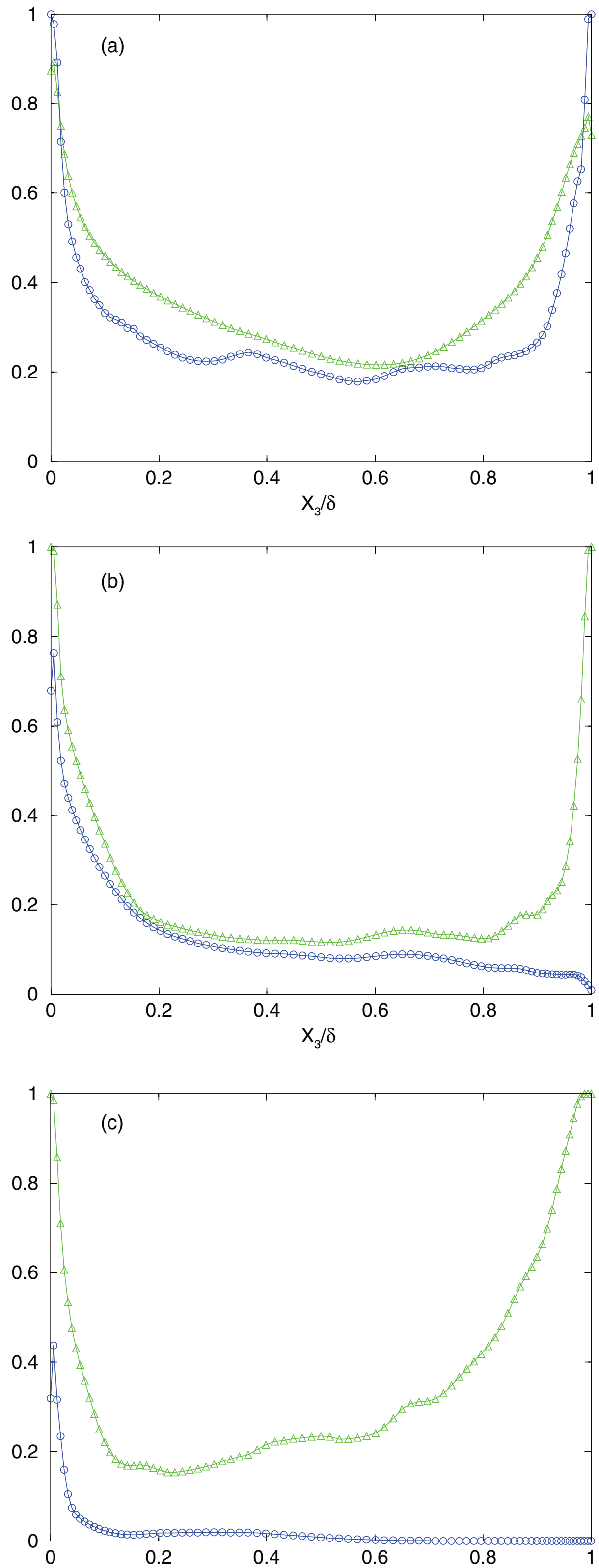

FIG. 14. Ratio of the subfilter energy to the total energy. Equilibrium ratio $\langle k_{SFS}\rangle/k = [1+\beta_\eta(\kappa_c L_e)^3]^{-2/9}$: $\triangle$; Computed ratio $\langle k_{SFS}\rangle/k$: $\circ$. (a) $R_o = 0.17$, (b) $R_o = 0.50$, (c) $R_o = 1.50$. PITM1 ($24 \times 48 \times 64$).

equation is directly affected by the rotation through the coefficient $c_{SFS\epsilon_2}$ which is a function of $\langle k_{SFS}\rangle/k$. In addition to the Coriolis forces that are embedded in the transport equations for the subfilter stresses as source terms, this is the reason which explains why the subfilter model is very sensitive to the rotation. This interdependence between the turbulent coefficients and the transport equations also induces a strong coupling between the turbulent stress field and the mean velocity.

F. Qualitative flow structures

Figures 15–17 show the isosurfaces of the instantaneous vorticity modulus for both the PITM1 and PITM2 simulations performed on the coarse and medium grids at different rotation rates $R_o = 0.17, 0.50, 1.50$ and also for the PITM3 simulation performed on the refined grid at the highest rotation rate $R_o = 1.50$. A first glimpse of sight reveals that the PITM2 and PITM3 simulations provide some dynamical elements of the flow in wall turbulence and clearly illustrate the three-dimensional nature of the flow although the geometry is two-dimensional. For the PITM1 simulations, these structures are not explicitly appearing on the coarse grid for the same value of the vorticity modulus. In fact, they are still present in the flow but are very weak and emerge at lower value of the vorticity modulus. Indeed, the more the grid is coarse, the more the flow structures are weak and smoothing varying, the mesh acting like a low-pass filter that reduces high frequencies. Obviously, the coarse and medium grids are not sufficiently refined in the streamwise and spanwise directions to get quantitative DNS or highly resolved LES results.[6] But it is remarkable that the present PITM simulations, in spite of their coarse grids, succeed in satisfactorily reproducing these structures from a qualitative point of view. As a result, the PITM3 simulation performed on the refined grid is able to quantitatively reproduce these dynamical structures at $R_o = 1.50$ because this one captures both

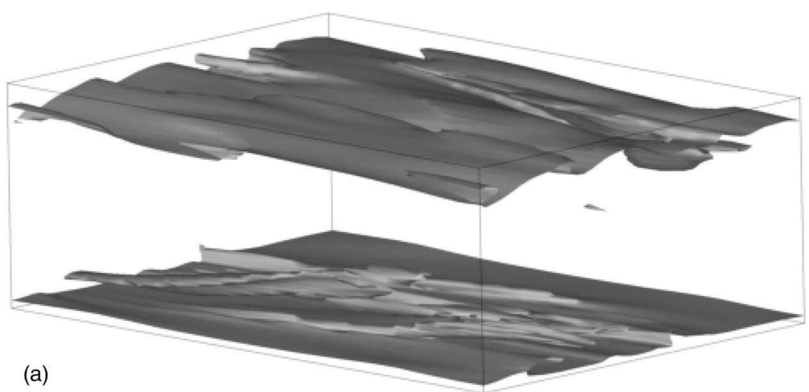

(a)

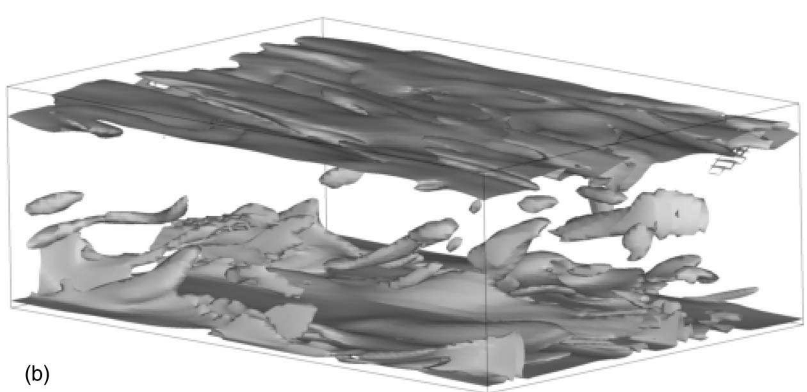

(b)

FIG. 15. Isosurfaces of vorticity modulus $\omega = 3u_m/\delta = 8 \times 10^5$. $R_m = 14\,000$, $R_o = 0.17$. (a) PITM1 ($24 \times 48 \times 64$); (b) PITM2 ($84 \times 64 \times 64$).

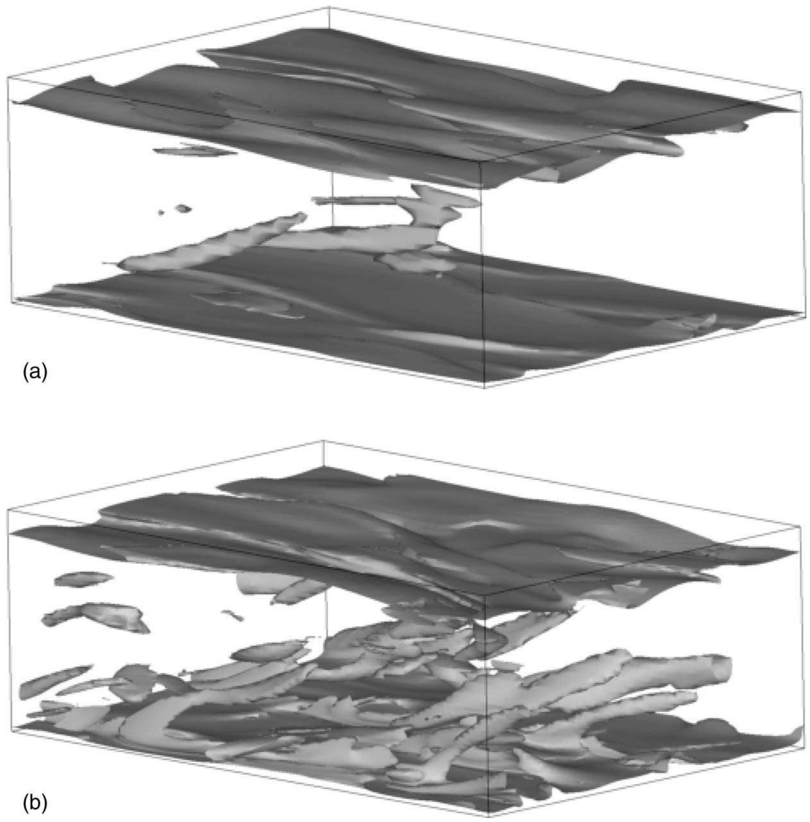

FIG. 16. Isosurfaces of vorticity modulus $\omega = 3u_m/\delta = 9 \times 10^5$. $R_m = 14\,000$, $R_o = 0.50$. (a) PITM1 ($24 \times 48 \times 64$); (b) PITM2 ($84 \times 64 \times 64$).

large scales and also smaller scales like the highly resolved LES (Ref. 6) due to the grid refinement effects. In that sense, it is clear that the PITM3 simulation reverts to standard highly resolved LES as the grid size is reduced. This result is not at all surprising since the subfilter model goes to the Smagorinsky model when η_c is large as demonstrated in references[4,49] using spectral equilibrium equations. When comparing these figures, on the one hand, one can see that the turbulence activity is gradually reduced near the cyclonic wall as the rotation rate is increased. On the other hand, a strong turbulence activity brought to light by the presence of very large-scale longitudinal roll cells, as previously observed by experimental flow visualization[8] and captured by highly resolved LES,[6] is visible in the anticyclonic wall region. The present investigation of the structural aspects of the flows provides some insights of the turbulence that correspond fairly well with the distribution of the turbulent energy in the channel. Figures 15–17 reveal other elements of interest concerning the development of the evolving flow structures. It appears that the flow becomes more and more organized as the rotation rate increases. In particular, this rotation effect is particularly visible at the highest rotation rate $R_o = 1.50$, as shown in Figure 17 describing quasi-organized longitudinal roll cells in the anticyclonic wall region. Although qualitative results are obtained for the PITM2 simulation, one can see that these vorticity roll cells appearing at the rotation rate $R_o = 1.50$ are less inclined with respect to the wall than those simulated at the lower rotation rates $R_o = 0.17$ and 0.50. This tendency of the rotation on the flow structures is physically well recovered by the PITM simulations. Indeed, as previously investigated by means of highly resolved LES,[6] the vorticity vectors are less inclined from 45° to 10°-15° when the rotation rate is increased from $R_o = 0$ to 1.50. On the basis of these elements, this section demonstrates in a practical point of view that the PITM method is basically different from the URANS approach. This one only provides mean organized structures because of its long time averaging.

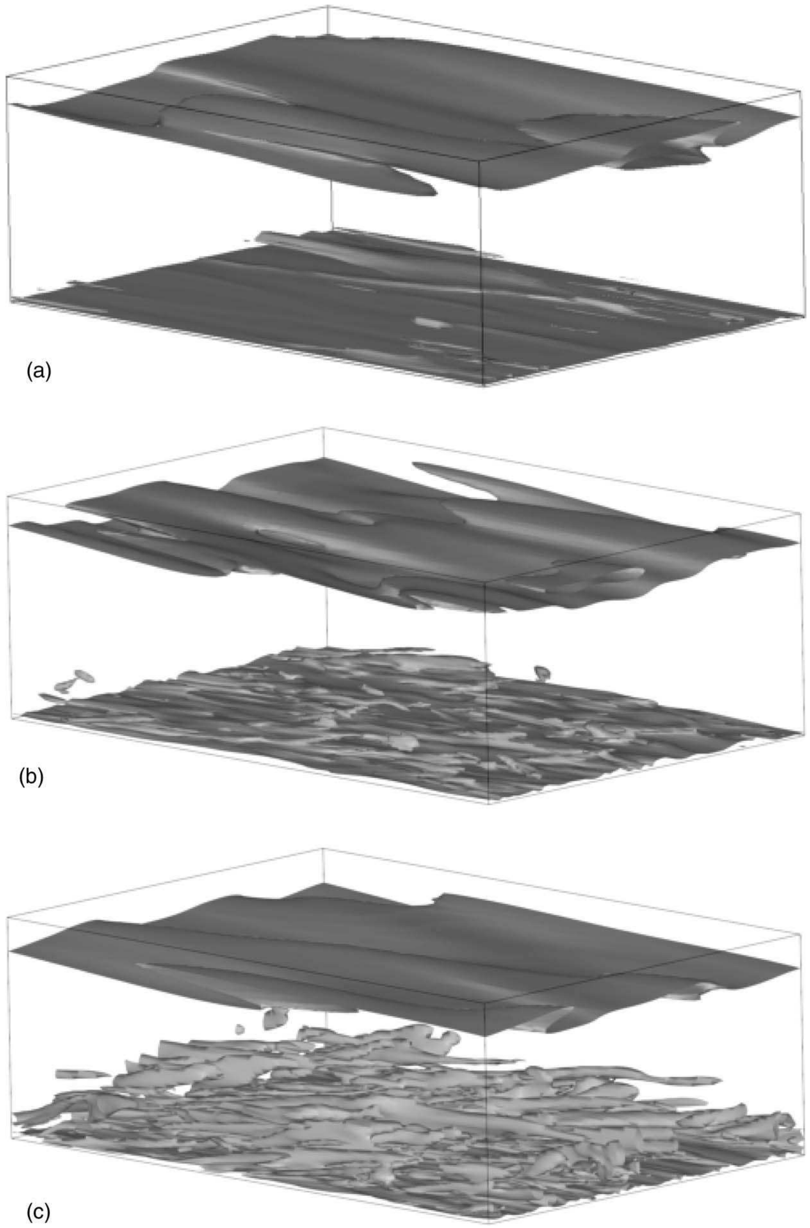

FIG. 17. Isosurfaces of vorticity modulus $\omega = 3u_m/\delta = 12 \times 10^5$. $R_m = 14\,000$, $R_o = 1.50$. (a) PITM1 ($24 \times 48 \times 64$); (b) PITM2 ($84 \times 64 \times 64$); (c) PITM3 ($124 \times 84 \times 84$).

VII. CONCLUDING REMARKS

The PITM method has been applied for devising a subfilter-scale stress model to account for rotation in the framework of SMC. In this study, the pressure-strain correlation term encompassed in this model has been inspired from the nonlinear SSG model[5] initially developed for homogeneous rotating flows in RANS methodology. The subfilter-scale stress model has been formulated especially in a low Reynolds number version for accurately capturing the mean velocity and turbulent stresses in the wall boundary layer. Then, it has been used for simulating large scales of rotating turbulent flows on coarse and medium grids at moderate, medium, and high rotation rates. As a result, it has been found that the PITM simulations have reproduced fairly well the mean features of rotating channel flows with a sufficient fidelity from an engineering point of view allowing in the present case a drastic reduction of the computational cost in comparison with those required for performing highly resolved LES. Overall, the mean velocities and turbulent stresses were found in good agreement with the data of highly resolved LES (Ref. 6) and the anisotropy character of the flow resulting from the rotational effects has been well reproduced in accordance with the reference data. The PITM2 simulations performed on the medium grid have qualitatively well predicted the three-dimensional flow structures including the longitudinal roll cells that develop in the anticyclonic wall-region. It is the feeling of the author that the present model can be used for simulating other complex flows encountered in turbomachinery industry, provided the numerical procedure is sufficiently robust to solve the system of transport equations.

APPENDIX: OBJECTIVITY OF THE PRESSURE-STRAIN CORRELATION TENSOR Π_{ij}

The question is to determine whether the exact and modeled pressure-strain tensors Π_{ij} are objective tensors in a mathematical sense. A tensor is said to be objective if it remains unchanged under an arbitrary dependent rotation and a translation of the spatial frame of reference given by

$$\boldsymbol{x}^* = \boldsymbol{Q}(t)\,\boldsymbol{x} + \boldsymbol{b}(t), \quad t^* = t + c, \tag{A1}$$

where c is a constant coefficient, $\boldsymbol{b}$ is a time-dependent vector, and $\boldsymbol{Q}$ is any time-dependent proper orthogonal tensor verifying the well-known relation,

$$\dot{Q}_{km} Q_{lm} = -\dot{Q}_{lm} Q_{km} = \epsilon_{mkl} \Omega_m, \tag{A2}$$

and implying that $\boldsymbol{Q}$ is an antisymmetric tensor.[16] In LES methodology[79–81] including the PITM method, the instantaneous velocity transforms as

$$u_i^* = Q_{im} u_m + \dot{Q}_{im} x_m + \dot{b}_i. \tag{A3}$$

The filtered velocity $\bar{u}_i$ is then obtained by applying the general definition (3)

$$\overline{u_i^*}(\boldsymbol{x}^*) = \iiint_{\mathcal{D}} G_\Delta(\boldsymbol{x}^* - \boldsymbol{x}'^*) \left[Q_{im} u_m + \dot{Q}_{im} x_m + \dot{b}_i \right] (\boldsymbol{x}'^*)\, d^3x'^*. \tag{A4}$$

If we restrict the filtering process to the particular case of isotropic filters,[79] the filtering process does not depend on the frame of reference, i.e., $G_\Delta(|\boldsymbol{x}^* - \boldsymbol{x}'^*|) = G_\Delta(|\boldsymbol{x} - \boldsymbol{x}'|)$. Then, the filtered velocity can be computed by means of a change of variable

$$\overline{u_i^*}(\boldsymbol{x}) = \iiint_{\mathcal{D}} G_\Delta(|\boldsymbol{x} - \boldsymbol{x}'|) \left[Q_{im} u_m + \dot{Q}_{im} x_m + \dot{b}_i \right] \left| \frac{\partial \boldsymbol{x}'^*}{\partial \boldsymbol{x}'} \right| (\boldsymbol{x}')\, d^3x', \tag{A5}$$

where $|\partial \boldsymbol{x}'^* / \partial \boldsymbol{x}'|$ denotes the determinant of the jacobian matrix. As $\boldsymbol{Q}$ is a proper orthogonal tensor, the determinant is equal to unity so that Eq. (A5) leads to the result

$$\overline{u_i^*} = Q_{im} \bar{u}_m + \dot{Q}_{im} \bar{x}_m + \dot{b}_i. \tag{A6}$$

Using the fact that G is an even function while x is an odd function, one can demonstrate that $\bar{x} = x$.[79] The subgrid fluctuating velocity is then obtained by subtracting Eq. (A6) from Eq. (A3) leading to the result

$$u_i'^* = Q_{im} u_m' \tag{A7}$$

showing that it is invariant. We will now establish the frame invariance of the exact pressure-strain correlation term given by Eq. (22). The pressure is frame-indifferent, the concept of force being frame-independent. So that we consider that $\overline{p^*} = \bar{p}$ and $p'^* = p'$. By using the chain rule of differentiation,

$$\frac{\partial}{\partial x_i^*} = \frac{\partial x_m}{\partial x_i^*} \frac{\partial}{\partial x_m} = Q_{im} \frac{\partial}{\partial x_m}, \tag{A8}$$

we obtain the expressions for the gradients of the mean and fluctuating velocities as follows:

$$\frac{\partial \overline{u_i^*}}{\partial x_j^*} = Q_{im} Q_{jn} \frac{\partial \bar{u}_m}{\partial x_n} + \dot{Q}_{im} Q_{jm}, \tag{A9}$$

and

$$\frac{\partial u_i'^*}{\partial x_j^*} = Q_{im} Q_{jn} \frac{\partial u_m'}{\partial x_n}. \tag{A10}$$

Because of Eq. (A2), the transformation of the mean strain term is then given by

$$\overline{S_{ij}^*} = Q_{im} Q_{jn} \overline{S}_{mn}. \tag{A11}$$

Like in RANS modeling,[82] it is then simple matter to show that the exact pressure-strain term Π_{ij}^* is an objective tensor since it obeys the tensorial rule transformation as follows:

$$\Pi_{ij}^* = \Phi(p^*, S_{ij}^*) = 2(\overline{p^* S_{ij}^*} - \bar{p^*} \overline{S_{ij}^*})/\rho = 2(\overline{p\, Q_{im} Q_{jn} S_{mn}} - \bar{p}\, \overline{Q_{im} Q_{jn} S_{mn}})/\rho = Q_{im} Q_{jn} \Pi_{mn}. \tag{A12}$$

Now, we examine the transformation of the modeled pressure-strain term $\Pi_{ij} = \Pi_{ij}(a_{ij}, S_{ij}, W_{ij})$ including the terms Π_{ij}^1 and Π_{ij}^2 defined by Eqs. (33) and (35) under the change of frame. This term Π_{ij}^* is determined by replacing a_{ij}, S_{ij}, and W_{ij} by a_{ij}^*, S_{ij}^*, and W_{ij}^*, respectively. Since the anisotropy tensor a_{ij} defined in Eq. (34) is computed with $(\tau_{ij})_{SFS}$, we need to compute first the subfilter stress tensor $(\tau_{ij}^*)_{SFS}$ under the change of frame. Applying the tensor rules given by Eq. (A6), it is found after some analytical developments that $(\tau_{ij})_{SFS}$ transforms as

$$\begin{aligned}(\tau_{ij}^*)_{SFS} = {} & Q_{im} Q_{jp} (\tau_{mp})_{SFS} + Q_{im} \dot{Q}_{jp} \left[\overline{u_m x_p} - \bar{u}_m x_p\right] + Q_{jm} \dot{Q}_{ip} \left[\overline{x_m u_p} - x_m \bar{u}_p\right] \\ & + \dot{Q}_{im} \dot{Q}_{jp} \left[\overline{x_m x_p} - x_m x_p\right]\end{aligned} \tag{A13}$$

showing that $(\tau_{ij}^*)_{SFS}$ is not an objective tensor in LES methodology. More precisely, Eq. (A13) indicates that it depends on the motion of the frame of reference through the rotation but is frame indifferent through the translation. But as the additional terms appearing in the right-hand side of Eq. (A13) are small in comparison with the first term, we can admit that the subfilter stress tensor $(\tau_{ij})_{SFS}$ transforms as

$$(\tau_{ij}^*)_{SFS} \approx Q_{im} Q_{jp} (\tau_{mp})_{SFS}. \tag{A14}$$

Using Eq. (A9), the absolute filtered vorticity tensor $\overline{W}_{ij}^*$ transforms as

$$\overline{W_{ij}^*} = Q_{im} Q_{jp} \overline{W}_{mp}, \tag{A15}$$

thanks to Eq. (A2). Taking into account Eqs. (A11), (A14), and (A15), we finally found that the modeled pressure-strain correlation term Π_{ij} transforms as

$$\boldsymbol{\Pi}^* = \boldsymbol{\Pi}(\boldsymbol{a}^*, \overline{\boldsymbol{S}^*}, \overline{\boldsymbol{W}^*}) = \boldsymbol{\Pi}(\boldsymbol{Q} \boldsymbol{a} \boldsymbol{Q}^T, \boldsymbol{Q} \overline{\boldsymbol{S}} \boldsymbol{Q}^T, \boldsymbol{Q} \overline{\boldsymbol{W}} \boldsymbol{Q}^T) \approx \boldsymbol{Q} \boldsymbol{\Pi}(\boldsymbol{a}, \overline{\boldsymbol{S}}, \overline{\boldsymbol{W}}) \boldsymbol{Q}^T. \tag{A16}$$

In a mathematical sense, Eq. (A16) indicates that the modeled term Π_{ij} is not an objective tensor but only an approximation. In the case where this approximation holds, Π_{ij} is an isotropic tensor function of its arguments.[83]

[1] B. Chaouat and R. Schiestel, "A new partially integrated transport model for subgrid-scale stresses and dissipation rate for turbulent developing flows," Phys. Fluids **17**, 065106 (2005).
[2] R. Schiestel and A. Dejoan, "Towards a new partially integrated transport model for coarse grid and unsteady turbulent flow simulations," Theor. Comput. Fluid Dyn. **18**, 443 (2005).
[3] B. Chaouat and R. Schiestel, "From single-scale turbulence models to multiple-scale and subgrid-scale models by Fourier transform," Theor. Comput. Fluid Dyn. **21**, 201 (2007).
[4] B. Chaouat and R. Schiestel, "Progress in subgrid-scale transport modelling for continuous hybrid non-zonal RANS/LES simulations," Int. J. Heat Fluid Flow **30**, 602 (2009).
[5] C. G. Speziale, S. Sarkar, and T. B. Gatski, "Modelling the pressure-strain correlation of turbulence: an invariant dynamical systems approach," J. Fluid Mech. **227**, 245 (1991).
[6] E. Lamballais, O. Métais, and M. Lesieur, "Spectral-dynamic model for large-eddy simulations of turbulent rotating flow," Theor. Comput. Fluid Dyn. **12**, 149 (1998).
[7] B. E. Launder, D. P. Tselepidakis, and B. A. Younis, "A second-moment closure study of rotating channel flow," J. Fluid Mech. **183**, 63 (1987).
[8] J. P. Johnston, R. M. Halleen, and D. K. Lezius, "Effects of spanwise rotation on the structure of two-dimensional fully developed turbulent channel flow," J. Fluid Mech. **56**, 533 (1972).

[9] B. A Pettersson and H. I. Andersson, "Near wall Reynolds stress modelling in noninertial frames of reference," Fluid Dyn. Res. **19**, 251 (1997).
[10] B. Chaouat, "Simulations of channel flows with effects of spanwise rotation or wall injection using a Reynolds stress model," ASME J. Fluids Eng. **123**, 2 (2001).
[11] S. Jakirlic, K. Hanjalic, and C. Tropea, "Modeling rotating and swirling turbulence flows: A perpetual challenge," AIAA J. **40**, 1984 (2002).
[12] T. B. Gatski and C. G. Speziale, "On explicit algebraic stress models for complex turbulent flows," J. Fluid Mech. **254**, 59 (1993).
[13] T. B. Gatski and S. Wallin, "Extending the weak-equilibrium condition for algebraic Reynolds stress models to rotating and curved flows," J. Fluid Mech. **518**, 147 (2004).
[14] T. Jongen, L. Machiels, and T. B. Gatski, "Prediction nonlinear effects with linear and nonlinear eddy-viscosity, and algebraic stress models," Flow, Turbul. Combust. **60**, 215 (1998).
[15] F. Hamba, "The mecanism of zero mean absolute vorticity state in rotating channel flow," Phys. Fluids **18**, 125104 (2006).
[16] R. Schiestel, *Modeling and Simulation of Turbulent Flows* (ISTE Ltd/Wiley, 2008).
[17] R. Kristoffersen and H. I. Andersson, "Direct simulations of low-Reynolds-number turbulent flow in a rotating channel," J. Fluid Mech. **256**, 163 (1993).
[18] E. Lamballais, O. Métais, and M. Lesieur, "Effects of spanwise rotation on the vorticity stretching in transitional and turbulent channel flow," Int. J. Heat Fluid Flow **17**, 324 (1996).
[19] H. Wu and N. Kasagi, "Effects of arbitrary directional system rotation on turbulent channel flow," Phys. Fluids **16**, 979 (2004).
[20] O. Grundestam, S. Wallin, and A. Johansson, "Direct numerical simulations of rotating turbulent channel flow," J. Fluid Mech. **598**, 177 (2008).
[21] G. Brethouwer, P. Schlatter, and A. V. Johansson, "Effects of rapid spanwise rotation on turbulent channel flow with a passive scalar," in *Proceeding of the 7th Symposium on Turbulent Shear Flow Phenomena*, edited by J. Eaton, R. Friedrich, J. Humphrey, A. Johanson, N. Kasagi and S. Tavoularis (Ottawa, 2011), No. 8B3P, pp. 1–6.
[22] D. K. Tafti and S. P. Vanka, "A numerical study of the effects of spanwise rotation on turbulent channel flow," Phys. Fluids A **3**, 642 (1991).
[23] U. Piomelli and J. Liu, "Large eddy simulations of rotating channel flows using a localized stress model," Phys. Fluids **7**, 839 (1995).
[24] M. Lesieur and O. Metais, "New trends in large-eddy simulations of turbulence," Annu. Rev. Fluid Mech. **28**, 45 (1996).
[25] J. Smagorinsky, "General circulation experiments with the primitive equations," Mon. Weather Rev. **91**, 99 (1963).
[26] M. Germano, U. Piomelli, P. Moin, and W. H. Cabot, "A dynamic subgrid-scale eddy-viscosity model," Phys. Fluids A **3**, 1760 (1992).
[27] M. Germano, "A statistical formulation of the dynamic model," Phys. Fluids **8**, 565 (1996).
[28] P. R. Spalart, "Detached-eddy simulation," Annu. Rev. Fluid Mech. **41**, 181 (2009).
[29] P. Mellen, J. Fröhlich, and W. Rodi, "Lessons from LESFOIL project on large-eddy simulation of flow around an airfoil," AIAA J. **41**, 573 (2003).
[30] B. E. Launder, G. J. Reece, and W. Rodi, "Progress in the development of a Reynolds stress turbulence closure," J. Fluid Mech. **68**, 537 (1975).
[31] S. Jakirlic and K. Hanjalic, "A new approach to modelling near-wall turbulence energy and stress dissipation," J. Fluid Mech. **459**, 139 (2002).
[32] R. Manceau and K. Hanjalic, "Elliptic blending model: A new near-wall Reynolds-stress turbulence closure," Phys. Fluids **14**, 744 (2002).
[33] B. Chaouat, "Reynolds stress transport modeling for high-lift airfoil flows," AIAA J. **44**, 2390 (2006).
[34] R. Kristoffersen, P. J. Nilsen, and H. I. Andersson, "Validation of Reynolds stress closures for rotating channel flows by mean of direct numerical simulations," in *Engineering Turbulence Modelling and Measurements*, edited by W. Rodi and E. N. Ganic (Elsevier, Dubrovnik, 1990), Vol. 1, pp. 55–64.
[35] M. L. Shur, M. K. Strelets, and A. K. Travin, "Turbulence modeling in rotating and curved channels: assessing the Spalart-Shur correcion," AIAA J. **38**, 784 (2000).
[36] J. B. Cazalbou, P. Chassing, G. Dufour, and X. Carbonneau, "Two-equation modeling of turbulent rotating flows," Phys. Fluids **17**, 055110 (2005).
[37] Y. Nagano and H. Hattori, "An improved turbulence model for rotating shear flows," J. Turbul. **3**, 006 (2002).
[38] T. B. Gatski, C. L. Rumsey, and R. Manceau, "Current trends in modelling research for turbulent aerodynamic flows," Philos. Trans. R. Soc. London, Ser. A **365**, 2389 (2007).
[39] M. Germano, *From RANS to DNS: Toward a Bridging Model*, Direct and Large-Eddy Simulation III, ERCOFTAC Vol. 7, edited by P. Voke, N. D. Sandham, and L. Kleiser (Kluwer Academic, 1999), pp. 225–236.
[40] P. Sagaut, S. Deck, and M. Terracol, *Multiscale and Multiresolution Approaches in Turbulence* (Imperial College, London, 2006).
[41] J. Fröhlich and D. Von Terzi, "Hybrid LES/RANS methods for the simulation of turbulent flows," Prog. Aerosp. Sci. **44**, 349 (2008).
[42] B. Aupoix, D. Arnal, H. Bézard, B. Chaouat, F. Chedevergne, S. Deck, V. Gleize, P. Grenard, and E. Laroche, "Transition and turbulence modelling," The ONERA J. Aerosp. Lab. **2**, 1 (2011).
[43] F. Hamba, "Analysis of filtered Navier-Stokes equation for hybrid RANS/LES simulation," Phys. Fluids **23**, 015108 (2011).
[44] M. L. Shur, P. R. Spalart, M. K. Strelets, and A. K. Travin, "A hybrid RANS-LES approach with delayed-DES and wall-modelled LES capabilities," Int. J. Heat Fluid Flow **29**, 1638 (2008).
[45] B. Chaouat, "Subfilter-scale transport model for hybrid RANS/LES simulations applied to a complex bounded flow," J. Turbul. **11**, 1 (2010).
[46] M. Germano, "Turbulence: the filtering approach," J. Fluid Mech. **238**, 325 (1992).

[47] I. Befeno and R. Schiestel, "Non-equilibrium mixing of turbulence scales using a continuous hybrid RANS/LES approach: Application to the shearless mixing layer," Flow, Turbul. Combust. **78**, 129 (2007).
[48] A. Fadai-Ghotbi, C. Friess, R. Manceau, T. B. Gatski, and J. Borée, "Temporal filtering: A consistent formalism for seamless hybrid RANS-LES modeling in inhomogeneous turbulence," Int. J. Heat Fluid Flow **31**, 378 (2010).
[49] A. Fadai-Ghotbi, C. Friess, R. Manceau, and J. Borée, "A seamless hybrid RANS-LES model based on transport equations for the subgrid stressses and ellipting blending," Phys. Fluids **22**, 055104 (2010).
[50] S. Jakirlic, S. Saric, G. Kadavelil, E. Sirbubalo, B. Basara, and B. Chaouat, "SGS modelling in LES of wall-bounded flows using transport RANS models: from a zonal to a seamless hybrid LES/RANS method," in *Proceeding of the 6th Symposium on Turbulent Shear Flow Phenomena*, edited by N. Kasagi, J. Eaton, R. Friedrich, J. Humphrey, A. Johansson, and H. Sung, (Seoul, 2009), Vol. 3, pp. 1057–1062.
[51] D. Jeong, Y. Choi, and J. Shin, "Hybrid RANS-LES approaches for the prediction of turbulent heat flux," *Proceeding 6th Symposium on Turbulent Shear Flow Phenomena*, edited by N. Kasagi, J. Eaton, R. Friedrich, J. Humphrey, A. Johansson, and H. Sung, (Seoul, 2009), Vol. 2, pp. 517–522.
[52] Y. Bentaleb and R. Manceau, "A hybrid RANS/LES formulation based on a two-equation subfilter model," *Proceeding of the 7th Symposium on Turbulent Shear Flow Phenomena*, edited by J. Eaton, R. Friedrich, J. Humphrey, A. Johanson, N. Kasagi, and S. Tavoularis (Ottawa, 2011), No. 9A4P, pp. 1–6.
[53] G. K. Batchelor, *An Introduction to Fluid Dynamics* (Cambridges University Press, Cambridges, 1967).
[54] C. G. Speziale, "Turbulence modeling in noninertial frames of reference," Theor. Comput. Fluid Dyn. **1**, 3 (1989).
[55] R. Schiestel, "Sur le concept d'échelles multiples en modélisation des écoulements turbulents. Part I," J. Mech. Theor. Appl. **2**, 417 (1983).
[56] R. Schiestel, "Sur le concept d'échelles multiples en modélisation des écoulements turbulents. Part II," J. Mech. Theor. Appl. **2**, 601 (1983).
[57] R. Schiestel and B. Chaouat, "On partially integrated transport models for subgrid-scale modelling," ERCOFTAC Bull. **72**, 49 (2007).
[58] A. Scotti, C. Meneveau, and D. K. Lilly, "Generalized Smagorinsky model for anisotropic grids," Phys. Fluids **5**, 2306 (1993).
[59] S. S. Girimaji, E. Jeong, and R. Srinivasan, "Partially averaged Navier-Stokes method for turbulence: Fixed point analysis and comparisons with unsteady partially averaged Navier-Stokes," ASME J. Appl. Mech. **73**, 422 (2006).
[60] J. W. Deardorff, "The use of subgrid transport equations in a three-dimensional model of atmospheric turbulence," ASME J. Fluids Eng. **95**, 429 (1973).
[61] R. S. Rogallo, "Numerical experiments in homogeneous turbulence," NASA Technical Memorandum 81315, 1981.
[62] R. Schiestel, "Study of one-dimensional spectral dynamic equations of the Reynolds stresses in homogeneous anisotropic turbulence: Application to split-spectrum modeling," In *Proceeding of the Summer Program, Center for Turbulence Research* (Stanford University, California, 1987), pp. 95–108.
[63] R. Schiestel, "Multiple-time scale modeling of turbulent flows in one point closures," Phys. Fluids **30**, 722 (1987).
[64] B. J. Daly and F. H. Harlow, "Transport equations in turbulence," Phys. Fluids **13**, 2634 (1970).
[65] J. Lumley and G. Newman, "The return to isotropy of homogeneous turbulence," J. Fluid Mech. **82**, 161 (1977).
[66] S. C. Crow, "Viscoelastic properties of the fine-grained incompressible turbulence," J. Fluid Mech. **33**, 1 (1968).
[67] C. G. Speziale and N. M. G. Mhuiris, "On the prediction of equilibrium states in homogeneous turbulence," J. Fluid Mech. **209**, 591 (1989).
[68] B. Chaouat, "Numerical predictions of channel flows with fluid injection using Reynolds stress model," J. Propul. Power **18**, 295 (2002).
[69] B. Chaouat and R. Schiestel, "Reynolds stress transport modelling for steady and unsteady channel flows with wall injection," J. Turbul. **3**, 1 (2002).
[70] B. Chaouat, "An efficient numerical method for RANS/LES turbulent simulations using subfilter scale stress transport equations," Int. J. Numer. Meth. Fluids **67**, 1207 (2011).
[71] B. Chaouat and R. Schiestel, "Hybrid RANS/LES modeling for non-equilibrium turbulent flows," in *Proceeding of the 5th Symposium on Turbulent Shear Flow Phenomena*, edited by R. Friedrich, N. Adams, J. Eaton, J. Humphrey, N. Kasagi, and M. Leschziner (Munich, 2007), Vol. 2, pp. 753–758.
[72] S. A. Apte and V. Yang, "A large-eddy simulation study of transition and flow instability in a porous-walled chamber with mass injection," J. Fluid Mech. **477**, 215 (2003).
[73] M. Breuer, N. Peller, C. Rapp, and M. Manhart, "Flow over periodic hills. Numerical and experimental study in a wide range of Reynolds numbers," Comput. Fluids **38**, 433 (2009).
[74] U. Piomelli and J. R. Chasnov, *Large Eddy Simulations: Theory and Applications, Turbulence and Transition Modelling*, edited by M. Hallback, D. Henningson, A. Johansson, and P. Alfredson (Kluwer, 1996), pp. 269–331.
[75] D. K. Lilly, "Numerical simulations of developing and decaying two-dimensional turbulence," J. Fluid Mech. **45**, 395 (1971).
[76] R. Moser, D. Kim, and N. Mansour, "Direct numerical simulation of turbulent channel flow up to $R_\tau = 590$," Phys. Fluids **11**, 943 (1999).
[77] O. Métais and M. Lesieur, "Spectral large-eddy simulation of isotropic and stably stratified turbulence," J. Fluid Mech. **239**, 157 (1992).
[78] D. J. Tritton, "Stabilization and destabilization of turbulent shear flow in a rotating fluid," J. Fluid Mech. **241**, 503 (1992).
[79] C. G. Speziale, "Subgrid scale stress model for the large-eddy simulation of rotating turbulent flows," Geophys. Astrophys. Fluid Dyn. **33**, 199 (1985).
[80] C. G. Speziale, "Galilean invariance of subgrid-scale stress models in the large-eddy simulation of turbulence," J. Fluid Mech. **156**, 55 (1985).

[81] Y. Shimomura, "A family of dynamic subgrid-scale models consistent with asymptotic material frame indifference," J. Phys. Soc. Jpn. **68**, 2483 (1999).
[82] T. G. Thomas and H. S. Takhar, "Frame-invariance of turbulence constitutive relations," Astrophys. Space Sci. **141**, 159 (1988).
[83] G. F. Smith, "On isotropic functions of symmetric tensor, skew-symmetric tensors and vectors," Int. J. Eng. Sci. **9**, 899 (1971).